

**ROLE OF POWDER BED  
THICKNESS AND DEPOSITION  
DIRECTION ON THE CORROSION  
BEHAVIOR OF SELECTIVE LASER  
MELTED (SLM) Ti-6Al-4V ALLOY:  
EXPERIMENTS AND SIMULATIONS**

**M.Tech. Thesis**

By

**CHAITANYA VISHWAKARMA**

**(1802105016)**



**DISCIPLINE OF METALLURGY  
ENGINEERING AND MATERIAL  
SCIENCE**

**INDIAN INSTITUTE OF  
TECHNOLOGY INDORE**

**JUNE 2020**



**ROLE OF POWDER BED  
THICKNESS AND DEPOSITION  
DIRECTION ON THE CORROSION  
BEHAVIOR OF SELECTIVE LASER  
MELTED (SLM) Ti-6Al-4V ALLOY:  
EXPERIMENTS AND SIMULATIONS**

**A THESIS**

*Submitted in partial fulfillment of the  
requirements for the award of the degree*

*of*

**Master of Technology**

By

**CHAITANYA  
VISHWAKARMA  
(1802105016)**



**DISCIPLINE OF METALLURGY  
ENGINEERING AND MATERIAL  
SCIENCE**

**INDIAN INSTITUTE OF TECHNOLOGY  
INDORE**

**JUNE 2020**



# INDIAN INSTITUTE OF TECHNOLOGY INDORE

## CANDIDATE'S DECLARATION

I hereby certify that the work which is being presented in the thesis entitled **Role of Powder Bed Thickness and Deposition Direction on the Corrosion Behavior of Selective Laser Melted (SLM) Ti-6Al-4V Alloy: Experiments and Simulations** in the partial fulfillment of the requirements for the award of the degree of **Master Of Technology in Metallurgy** and submitted in the discipline of **Metallurgy engineering and Material science, Indian Institute of Technology Indore**, is an authentic record of my own work carried out during the time period from June 2019 to June 2020 under the supervision of Dr. K. Eswara Prasad, Assistant Professor, Discipline of Metallurgy Engineering and Material Science, Indian Institute of Technology Indore.

The matter presented in this thesis has not been submitted by me for the award of any other degree of this or any other institute.

*Chaitanya Vishwakarma*  
25/06/2020

**Signature of the student with date**  
**(CHAITANYA VISHWAKARMA)**

-----  
This is to certify that the above statement made by the candidate is correct to the best of my/our knowledge.

Signature of the Supervisor of M.Tech. thesis  
**(Dr. K. Eswara Prasad)**

*K Eswara Prasad*  
25/06/2020

-----  
**CHAITANYA VISHWAKARMA** has successfully given his/her M.Tech. Oral Examination held on 25/06/2020

Signature of Supervisor of M.Tech. thesis      Convener, DPGC

*K Eswara Prasad*  
25/06/2020

Signature of PSPC Member #1

*Dr. K. Eswara Prasad*

Signature of PSPC Member #2

*Dr. K. Eswara Prasad*  
26/06/2020

## **ACKNOWLEDGEMENTS**

It is a pleasure to thank many people who made this work possible. First and foremost, I would like to thank my advisor, Dr. K. Eswara Prasad for believing in me to carry out this work under his supervision. His constant encouragement, friendly interactions and constant support have enabled this work to achieve its present form. He is one of the best teacher I have come across in my life.

I would like to take this opportunity to thank my PSPC members Dr. Vinod Kumar and Dr. Indrasen Singh for their valuable time in assessing my work during the mid-term and end-term presentations and giving me valuable suggestions related to my work.

I am thankful to Dr. Vinod Kumar, Head of the Department- MEMS for providing facilities that I required throughout the M Tech work. I am also thankful to the faculty of this Department for their support and effort in teaching the concepts in Metallurgy Engineering.

I would like to express our thanks to Prof. U. Ramamurty, NTU Singapore for lending the material used in this work and Prof. Srikanth Gollapudi, IIT Bhubaneswar for allowing me to use Corrosion testing facility.

I sincerely thank Dr. Vinod Kumar for extending facilities of Nonequilibrium processing lab, Department of Metallurgy engineering and Material science, IIT Indore for carrying out metallographic sample preparation and optical microscope characterization.

I thank all my colleagues - Tulika Dixit, Abhinav Sharma, Vaibhav Kathvate, Janmejai, Darshan, Dheeraj, Akshay for helping me out with experiments and materials. I also thank Tulika dixit and Abhinav Sharma for their suggestions during writing the thesis. I thank my classmates and friends at the Institute for the good time I had here.

Finally, I thank my parents for their constant support.

## **DEDICATION**

I dedicate this work to Lord Hanuman, my guide, my parents, my sisters and my lovely nephew who always support me during my crucial moments.

# ABSTRACT

Additive Manufacturing (AM) or rapid prototyping or 3D printing is an advanced manufacturing technique for producing near net shape components with minimal finishing operations unlike the subtractive manufacturing routes. One of the unique advantage of this method, in contrast to the conventional manufacturing techniques is Its capability to fabricate parts directly from computer-aided design (CAD) data. Selective laser melting (SLM) is one of the several AM techniques which selectively melts the powder bed (layer by layer) to obtain the neat net shape components. Besides the ease of the manufacturing, SLM can generate lots of microstructural architectures and intricate shapes and hence one of the most popularly used AM method. Many of the metals and alloys such as steels, Al alloys, Ti alloys have been manufactured using SLM techniques whose mechanical properties have been investigated quite extensively. In the current work, our focus is to investigatethe corrosion response of Ti-6Al-4V alloys manufactured via SLM method.

Titanium and its alloys have widespread applications in lightweight structural applications due to their high specific strength (almost comparable to superalloys), elevated temperature mechanical properties, good corrosion resistance (even for saline water), bio-compatibility and non-magnetic properties. These properties make them suitable candidates for aerospace applications, chemical processing plants, biomedical applications. the Ti-6Al-4V is an  $\alpha+\beta$  titanium alloy comprising of 6% Al and 4% V is most widely used for industrial applications due to its excellent mechanical properties compared to the other Ti alloys.

Corrosion is an ever-present problem in all different environments, particularly in marine, bio-implant, and aviation applications. In this work, corrosion behavior of Ti-6Al-4V alloy manufactured using SLM technique with layer thickness of 30  $\mu\text{m}$  and 60  $\mu\text{m}$  with scan rotation  $67^\circ$ , was investigated. The change in thickness has a marked effect on

the microstructure on the microstructure and hence the corrosion properties. Electrochemical results show that 3067 samples have a higher corrosion rate than the B6067. Further corrosion simulations were conducted using COMSOL Multiphysics software and compared with the experimental results.



2.2 Corrosion studies on SLM Ti-6Al-4V alloys.....	19
2.2.2 Summary.....	20
2.3 Open questions.....	20
<b>3. Objective of Work.....</b>	<b>21</b>
<b>4. Materials and Experiments.....</b>	<b>22</b>
4.1 Materials used in the current study.....	22
4.2 Experiments.....	22
4.2.1 Microscopic examination.....	22
4.2.2 Electrochemical Measurements.....	23
4.2.3 Corrosion Rate Calculation.....	24
<b>5. Modelling Methodology.....</b>	<b>25</b>
5.1 Governing Equation.....	25
5.2 Geometry and Boundary Conditions.....	27
<b>6. Results and Discussions.....</b>	<b>30</b>
6.1. Microstructure and features.....	30
6.2. Tafel and other relevant plots and their description.....	32
6.3 Electrolyte potential obtained from corrosion simulation.....	34
6.4 Electrolyte current density obtained from corrosion simulation.....	38
6.5. Mesh sensitivity results.....	42
6.6. Comparison of experiment and simulation results.....	45
<b>7. Conclusions and Future Scope.....</b>	<b>47</b>
<b>8. References.....</b>	<b>49</b>

# LIST OF FIGURES

Figure 1.1 Steps involved in Additive Manufacturing [3].....	1
Figure 1.2 Classification of metal additive manufacturing technologies [3].....	3
Figure 1.3 Schematic diagram of WLAM [5].....	4
Figure 1.4 Schematic diagram of EBAM [5].....	5
Figure 1.5 Schematic diagram of WAAM [5] .....	5
Figure 1.6 Schematic diagram of SLM [9] .....	7
Figure 1.7 Aluminium fuselage of aeroplane made by SLM [3].....	8
Figure 1.8 Medical industry [3] .....	9
Figure 1.9 Classification of engineering metals based on the density and unique properties of Titanium [10] .....	11
Figure 1.10 Applications of Ti alloys a) bioimplants [10] b) aerospace jet engine [10] .....	11
Figure 1.11 Allotropic forms of Ti (a) HCP below 882°C and (b) BCC above 882°C along with the close-packed planes [10] .....	12
Figure 1.12 Phase diagram of Ti alloys indicating the role of alloying elements on stabilization of $\alpha$ and $\beta$ phases [10] .....	12
Figure 1.13 Phase diagram of Ti-6Al-4V alloys with solution treatment [10].....	13
Figure 1.14 Optical microstructures of a) Rolled b) Extruded c) SEM image of forged Ti64 alloy .....	14
Figure 1.15 Optical microstructures of a) SLM b) SLM+HT1 c) SLM+HT2 [16].....	15

Figure 1.16 Optical microstructures of a) Rolled b) WAAM c) SLM d) DED [16].....	16
Figure 5.1 Schematic of 2D meshed geometry in COMSOL Multiphysics.....	28
Figure 6.1 Optical microstructures of a) B3067, b) S3067, c) B6067, d) S6067. Dashed lines in (a) , (b), (c), and (d) are for ‘guiding the eye’ purpose.....	31
Figure 6.2 Potentiodynamic polarization curve for SLM manufactured Ti-6Al-4V alloys (a) Corrosion rate comparison (b) .....	33
Figure 6.3 Electrolyte potential of samples at two extreme values of applied voltage (a, b) B3067, (c,d) S3067, (e,f) B6067 , (g,h) S6067.	37
Figure 6.4 Electrolyte current density for samples at two extreme values of applied voltage (a, b) B3067, (c, d) S3067, (e, f) B6067, (g, h) S6067 .....	41
Figure 6.5 Schematic of 2D geometry with a) Coarser mesh b) Finer mesh c) comparison in polarization curve .....	44
Figure 6.6 Potentiodynamic polarization curve for SLM manufactured Ti-6Al-4V alloys (a) Corrosion rate comparison (b) .....	46

# LIST OF TABLES

Table 1. Comparison between energy sources used in metal additive manufacturing. ....	6
Table 2. Calculation of Equivalent Weight (EW).....	24
Table 3. Input parameters required for corrosion simulation of SLM manufactured Ti-6Al-4V alloys .....	29
Table 4. Computation time taken by coarser mesh and finer mesh .....	42
Table 5. Summary of corrosion current density and corrosion rate for SLM Ti-6Al-4V alloy in this study.....	44



# 1. Introduction

## 1.1 Additive manufacturing

Additive Manufacturing (AM) is a new advanced technique for manufacturing the 3D products using layer by layer material deposition [1]. Earlier it was known as Rapid Prototyping (RP), Rapid Tooling (RT), and Layered Manufacturing (LM). It is capable to fabricate parts directly from CAD data (computer-aided design) [2]. There are various steps involve in AM, firstly a computerized 3D model is developed and then convert it into Standard Tessellation/Triangulation Language (STL) file format or other compatible AM formats. Further, this file transfer to an AM machine for controlling the orientation and position of the part then, at last, the part is manufactured in AM machine. Figure 1.1 illustrates the steps involved in the AM process chain. The evolution of AM is happened in three phases: First one is manual prototyping where prototypes are not very sophisticated and products are not very complex. Second one is virtual prototyping started between 1975-1980 during which the computer was used for modeling and testing of the product so that the level of complexity of products is increased twice as compared to the previous stage [3]. The third one is rapid prototyping, which started in the mid-1980s, which uses the hard prototype lead to substantial reduction in the manufacturing time and increase in the complexity much higher than the second stage [3].

AM has seen rapid industrial growth over the last two decades. It started with Stereolithography (SLA) in the 1980s by Charles Chuck Hull [3]. Then, Deckard and Beaman started working on selective laser sintering (SLS) machine at Texas A&M University, USA. After this, the first fused deposition modeling (FDM) machine was developed by Scott Crump and his wife Lisa Crump while manufacturing a toy (frog) for their daughter [3]. AM has started with simple rapid prototyping and now it is developed to fabricate customized products with high complex

geometries. Due to this, AM has been considered as alternating route for fabricating parts in different applications, especially in aerospace, automobile, and biomedical industries [4]. The primary advantages of AM are high precision, fast manufacturing, and waste reduction as compared to the traditional manufacturing methods. Besides these advantages, the 3D printer is independent of the product geometry and hence removes the additional finishing operations [5]. Most of the materials used in early AM were polymer, plastic and ceramic but now-a-days metal AMs is increasingly becoming popular due to availability of several alloy raw materials. The usage of manufacturing technologies is subordinate to the raw material status during 3D metal printing [6].

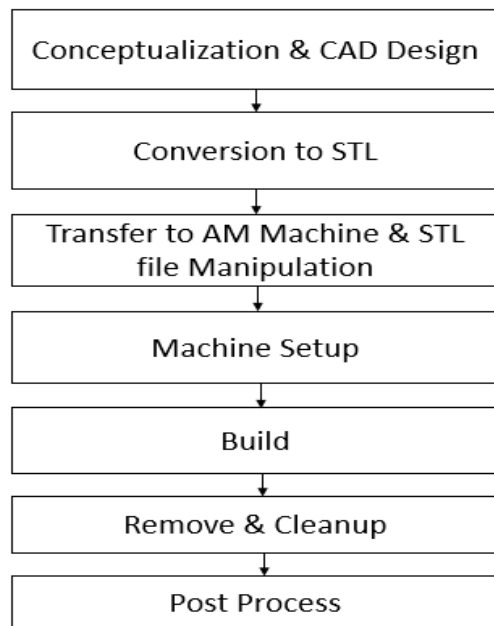


**Figure 1.1 Steps involved in Additive Manufacturing [3]**

## 1.2 Classification of various AM processes

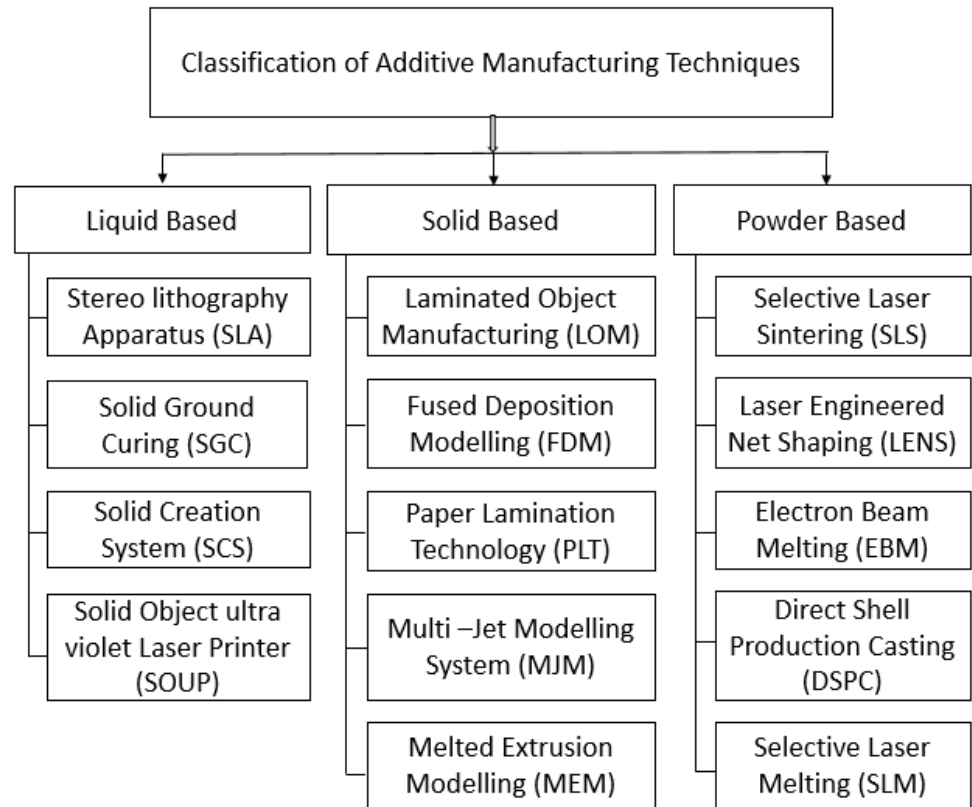


**Figure 1.2 Classification of metal additive manufacturing technologies [3]**

Among these technologies, the solid (wire-based) method has an advantage over the other two methods in terms of deposition rate and structural efficiency. Wire based methods also suitable for continuous and uncluttered material flow. Hence, the wire-based method is the most suitable for the fabrication of costly components [7]. One of the limitations of solid based methods is that they can not generate different microstructural architectures.

Based on the power source used, metal AM processes can be also classified as:

1. Wire and Laser-Based Additive Manufacturing (WLAM)
2. Electron Beam Additive Manufacturing (EBAM)

### 3. Wire and Arc Based Additive Manufacturing (WAAM)

#### 1.2.1 Wire and Laser-Based Additive Manufacturing (WLAM)

WLAM is a process of fabricating 3D complex shape products with the help of laser which is used as a heat source by continuous wire feed. In WLAM fabrication of small to medium scale parts with good quality and High density is possible. The only limitation of this method is the inability to produce large components and high operating cost compared to the traditional manufacturing methods [5].

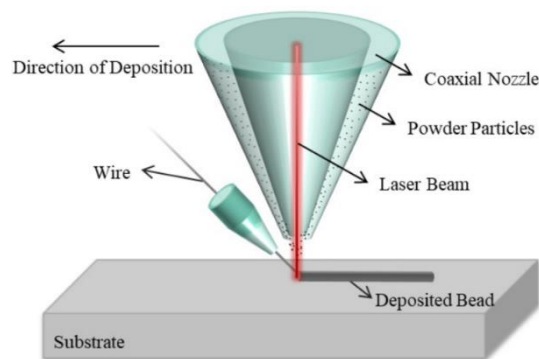


**Figure 1.3 Schematic diagram of WLAM [5]**

#### 1.2.2 Electron Beam Additive Manufacturing (EBAM)

This method allows the fabrication of large size, intricate and complex parts with the help of an electron beam as the heat source. In EBAM, the use of vacuum allows the easy deposition of reactive metals like titanium. EBAM is classified into two types - wire-based and powder-based. Wire based EBAM is simple to operate and has high deposition rates compared to powder-based EBAM. EBAM is costlier than WAAM due to the use of vacuum, it is heavy and expensive [8].

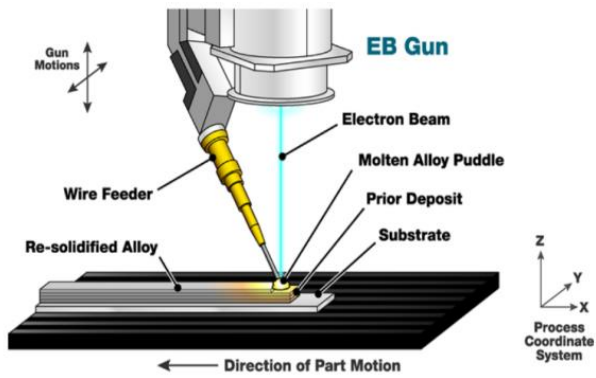


**Figure 1.4 Schematic diagram of EBAM [5]**

### 1.2.3 Wire and Arc Based Additive Manufacturing (WAAM)

In this technique fabrication of 3D parts carried out with the help of welding torch to generate weld pool by selecting optimum process parameters and adaptive tool path generating strategy. MIG welding torch is used for melting the wire and deposition is processed in the form of layers. WAAM is effective in fabricating larger and complex shape parts at a low cost. Due to the ability to change deposition parameters like voltage, current, and wire feed rate, etc. during the process it is possible to tailor the properties at desired locations by controlling the process parameters. The main advantage of WAAM over other processes is the high deposition rate which makes this method faster and compatible [8].

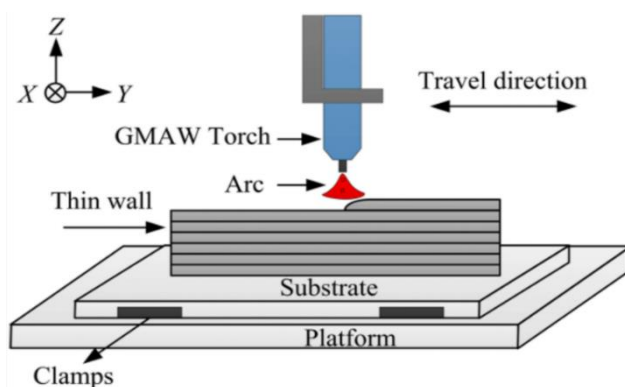


**Figure 1.5 Schematic diagram of WAAM [5]**

**Table 1.** Comparison between energy sources used in metal additive manufacturing.

<b>Characteristics</b>	<b>WLAM</b>	<b>EBAM</b>	<b>WAAM</b>
Size	Bulky	Bulky	Compact
Cost	Too Expensive	Too Expensive	Less Expensive
Speed	2 g/min	10 g/min	50-130 g/min
Material utilization	10-15 %	10-15 %	Close to 100%
Power Efficiency	2-5%	15-20%	>80%
Source	Photon	Electron	Metallic
Reactive metals	No	Yes	No

### **1.3 Selective Laser Melting (SLM) or Laser Beam Melting**

SLM is a powder-based AM method one of the which produces high-performance parts in a layer-wise manner directly from the CAD model. In this method, a powder layer is first distributed over a building platform with a powder depositer and a high intense laser beam selectively heats and melts the powder layer. After selective melting of the first layer. The entire platform is lowered by 20 to 100 microns and a new powder layer is distributed over the platform on which the laser scanning is performed. These steps are repeated until the desired product is obtained. In this, the melting of powder and cooling of molten pool occurs pool occurs rapidly which leads to the formation of significant amount of metastable or non-equilibrium phases which often causes a large amount of internal stresses. Due to these the components made after this are subjected to the stress relief annealing. Despite this, the metastable phases have a pronounced effect on the corrosion of SLM manufactured samples [9].

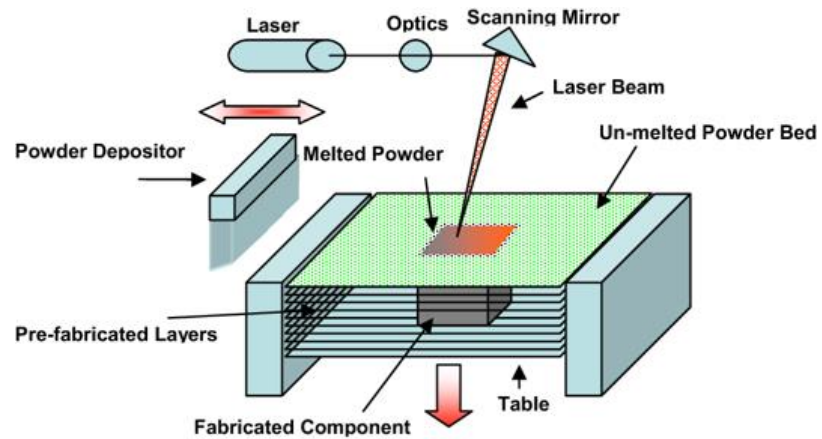


**Figure 1.6 Schematic diagram of SLM [9]**

### **1.3.1 Advantages, Limitation and Applications of SLM**

#### **Advantages**

- The part complexity is nearly unlimited.
- Parts or products can be printed rapidly.
- Decrease time to market.
- The dimensional accuracy is greater than 0.1 mm.

#### **Limitations**

- Materials diversity is limited.
- Good quality of laser and high laser power is required.
- Not suitable for the layer thickness of more than 0.2 mm
- Instabilities in melt pool and excessive residual stresses.

#### **Applications**

##### **1. Aerospace Industries**

Titanium, nickel, and aluminium alloys are the primary material used in the Aerospace industry and manufacturing of components from these materials with high complexity is the main challenge. A study shows that titanium components manufactured via forging technique requires removal of large amount of materials during the machining operation (90% weight) and hence making is more inviable [8].



**Figure 1.7 Aluminium fuselage of aeroplane made by SLM [3]**

## **2. Nuclear Industry**

High heat resistance, as well as corrosion resistance alloys such as nickel-based alloys and stainless steels, are commonly utilized in the nuclear industry can also be printed using SLM. Another advantage of SLM is the defected portion of a component can be repaired easily and create heat resistant microstructures in the regions by changing the processing parameters [8].

## **3. Medical Industry**

Chromium, titanium, and cobalt are the common material used for the fabrication of human vertebra, dental implants, treatment of bone fracture, and hip stem implants by SLM. But the magnesium alloys still require improvement in properties like biocompatibility and corrosion resistance to be used in SLM. Once these properties related problems are eliminated then parts fabricated through this technology can be easily used in the fabrication of medical components [8].

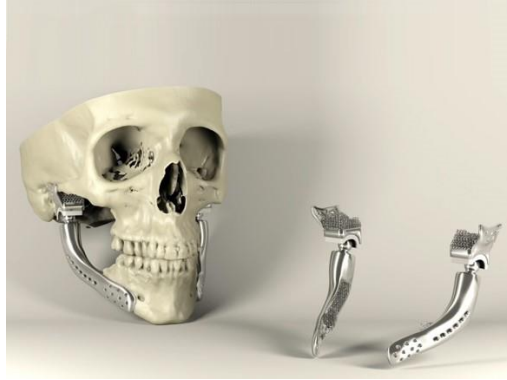


**Figure 1.8 Medical industry [3]**

## **1.4 Introduction to Titanium (Ti) and Ti alloys**

Titanium and its alloys have widespread usages in the lightweight structural applications due to their high specific strength (almost comparable to superalloys), elevated temperature mechanical properties, good corrosion resistance (even for saline water), biocompatibility and non-magnetic properties. These properties make them suitable candidates for aerospace applications, chemical processing plants, biomedical applications [10] as shown in Figure 1.10.

### **1.4.1 Crystal structures of Ti and the role of alloying elements**

At room temperature, Ti exhibits hexagonal close-packed (HCP) crystal structure and upon heating, it undergoes an allotropic transformation from HCP  $\alpha$  phase to body-centered cubic (BCC)  $\beta$  phase above 882°C as shown in Figure 1.11, The  $\alpha$ -Ti has limited number of independent slip systems (less than 5) and thus making it more brittle while the BCC phase has good ductility. Ti is highly reactive to Oxygen and Hydrogen causing its embrittlement at a higher temperature, therefore, Ti cannot be used in pure form in most of the engineering applications. Alloying Ti with other elements improves its properties. The transformation temperature,  $T_{tr}$ , is affected by the addition of substitutional and interstitial alloying elements. The alloying elements such as Boron, Oxygen, Nitrogen, Aluminium, Carbon stabilizes the  $\alpha$ -phase by increasing the  $T_{tr}$  above 882°C and hence are known as  $\alpha$ -stabilizers

while elements such as Vanadium, Molybdenum, Niobium increases the stability of  $\beta$  phase by reducing the  $T_{tr}$ . Few elements like Zr and Hf stabilizes both  $\alpha$  and  $\beta$  phases and hence are referred to as neutral stabilizers. At low concentrations, these stabilize the  $\alpha$ -phase while at high concentrations stabilize the  $\beta$  phase [10]. (Figure 1.12)

#### **1.4.2 Features of Ti-6Al-4V alloys**

Ti-6Al-4V (hereafter referred to as Ti64) alloy is an alpha - beta titanium alloy consists of 6% Al and 4% V. It is oldest and most used titanium alloy occupied around 50% of whole Ti and Ti alloys in various industries. Ti64 consists of a mixture of alpha and beta phases with the beta phase accounting for 10-15 % at room temperature. . In Ti64 alloys,  $\alpha$  phase contains higher percentage of Al which is also a  $\alpha$  phase stabilizer and has HCP crystal structure. while  $\beta$  phase contains higher percentage of V which is also a  $\beta$  phase stabilizer and has BCC crystal structure. Al and V increases some important properties of Ti64 alloy which are as follows : Al imparts higher creep resistance as well as high ductility while V imparts the high corrosion resistance. This alloy has low density, room and elevated temperature strength, fatigue and fracture resistance and it also exhibits superior corrosion resistance due to the formation of a passive film and have applications in the aerospace and medical industries Figure 1.9 shows a comparative chart of specific strength of Ti64 with other alloys. [10]

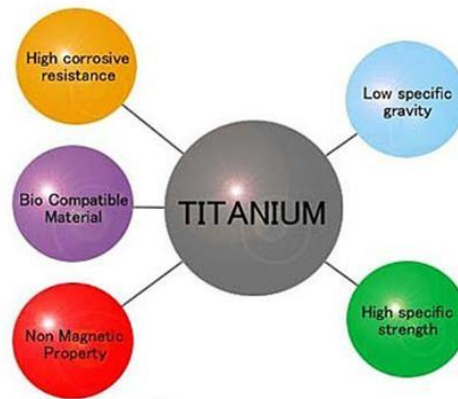
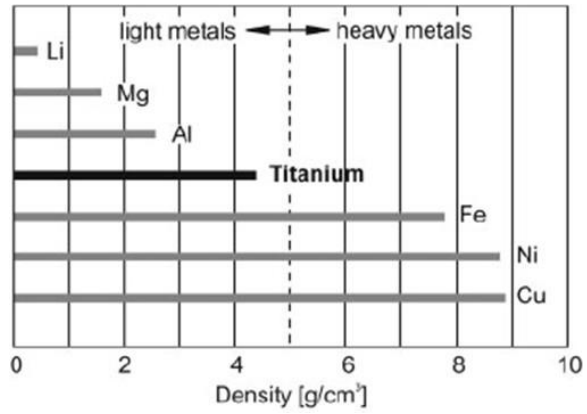


**Figure 1.9 Classification of engineering metals based on the density and unique properties of Titanium [10]**

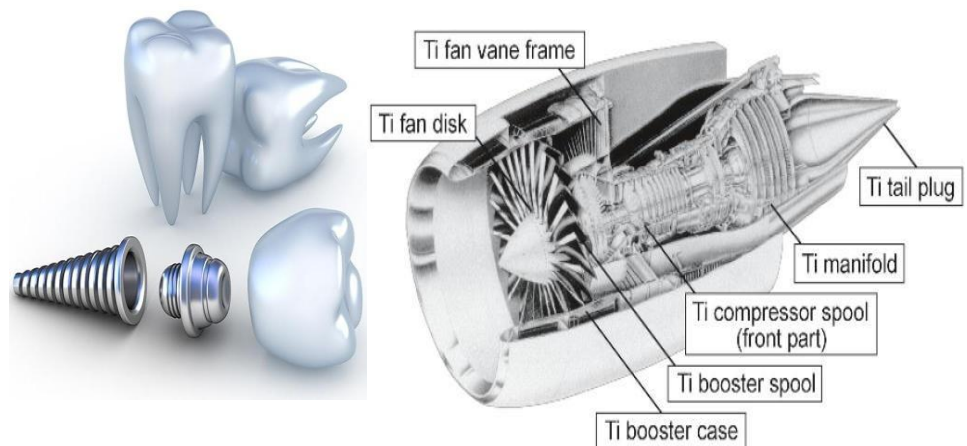


**Figure 1.10 Applications of Ti alloys a) bioimplants [10] b) aerospace jet engine [10]**

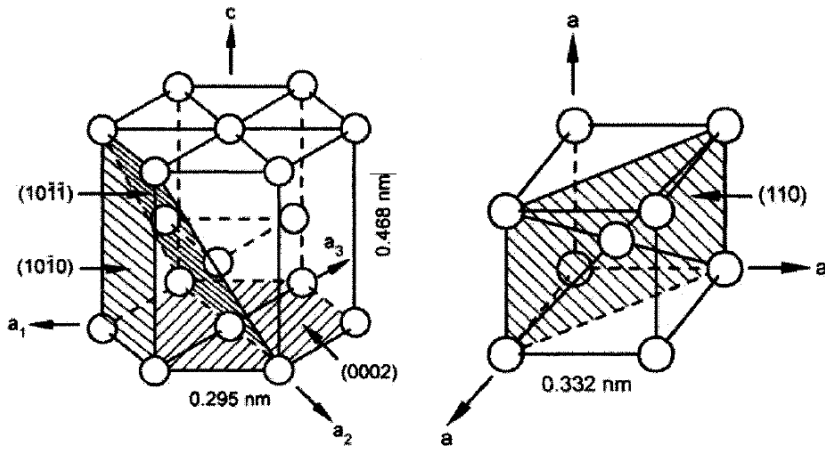


Figure 1.11 Allotropic forms of Ti (a) HCP below 882°C and (b) BCC above 882°C along with the close-packed planes [10]

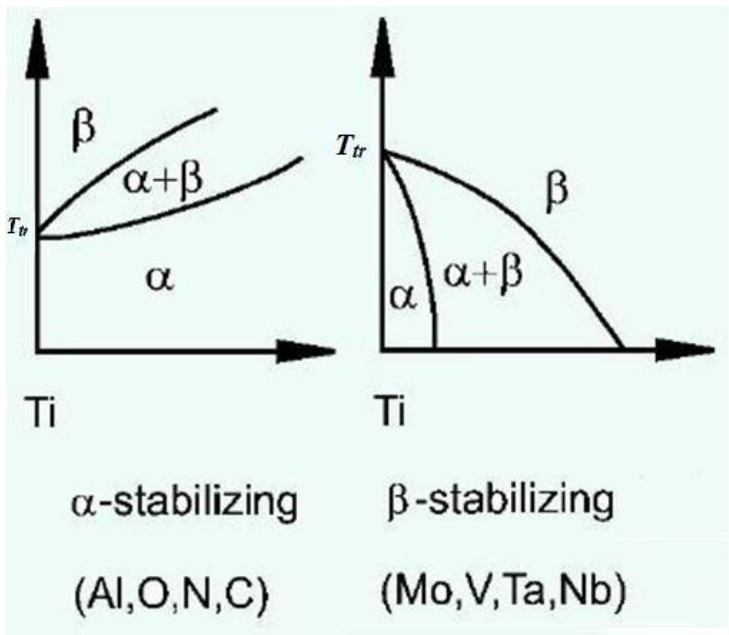
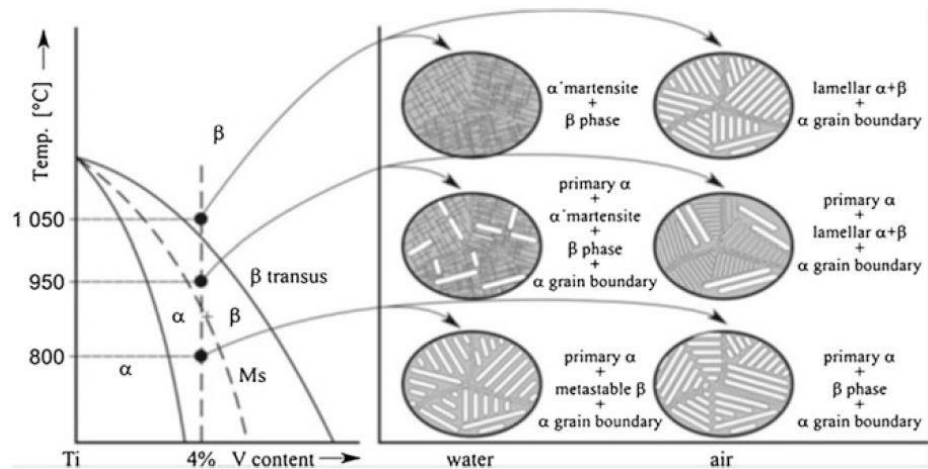


Figure 1.12 Phase diagram of Ti alloys indicating the role of alloying elements on stabilization of  $\alpha$  and  $\beta$  phases [10]

### 1.4.3 Phase diagram of Ti-6Al-4V alloys

Figure 1.13 represents the binary phase diagram of Ti-6Al-4V alloy with Ti-6Al is fixed at one axis and vanadium is varying at another axis. The maximum solubility limit of Al in titanium is 6 % and while the maximum solubility limit of V in Ti-6Al is 16 % at room temperature. The end microstructures depend on the cooling rate which is generally achieved by changing the cooling media. On cooling from 1050 °C, water quenching leads to formation of  $\alpha'$  martensite and  $\beta$  phase while lamellar  $\alpha+\beta$  and  $\alpha$  grain boundary were found in air cooling. On cooling below the martensite start temperature line at 800°C, primary  $\alpha$ , metastable  $\beta$  and  $\alpha$  grain boundary was found in water quenching but air-cooling leads to the formation of  $\alpha$  grain boundary, primary  $\alpha$ , and  $\beta$  phase [11].



**Figure 1.13 Phase diagram of Ti-6Al-4V alloys with solution treatment [11]**

#### 1.4.4 Wrought processed Ti64 alloys and common microstructures

Figure 1.14 (a) and (b) shows optical microstructures of rolled, extruded Ti64 alloy respectively. The rolled alloy comprises of equiaxed primary  $\alpha$  phase evenly distributed in the  $\alpha/\beta$  lamellae matrix [12] while extruded Ti64 alloy consists of severely elongated primary  $\alpha$  grains in a matrix of transformed  $\beta$  consisting of  $\beta$  in a matrix of non-plate-like  $\alpha$  [13]. Figure 1.14 (c) shows the SEM image of forged Ti64 alloy which mainly consists of an equi-axed  $\alpha$  primary nodules, decorated at grain boundaries by the  $\beta$  phase [14].

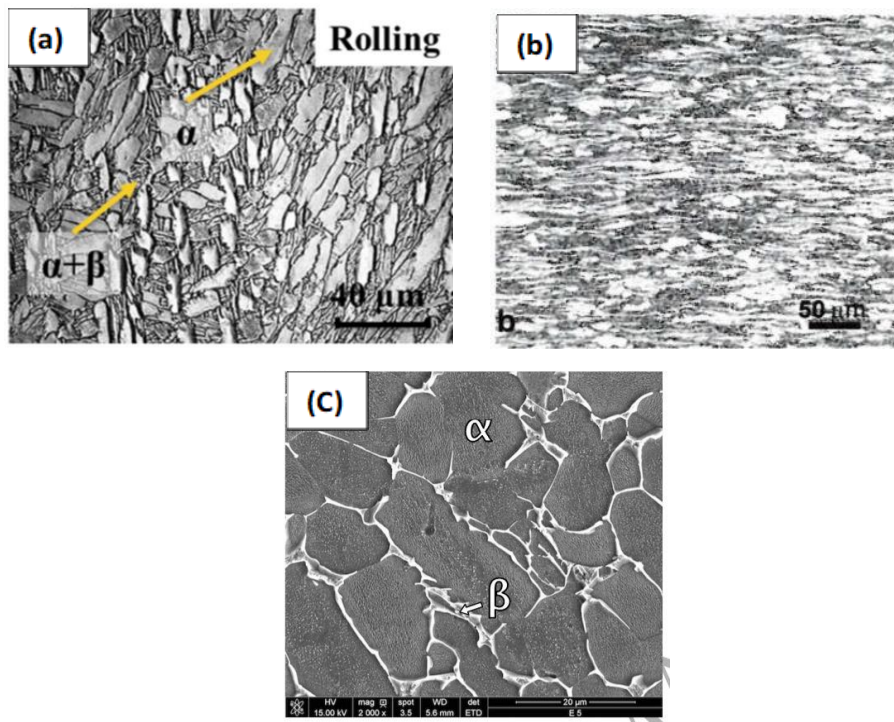


**Figure 1.14 Optical microstructures of a) Rolled [12] b) Extruded [13] c) SEM image of forged Ti64 alloy [14]**

### 1.4.5 SLM of Ti64 alloys and typical microstructures

Figure 1.15 (a) shows the optical microstructure of SLM Ti64 alloys, consists of metastable or non-equilibrium acicular  $\alpha'$  martensite phase and some or a negligible amount of  $\beta$  phase. This non-equilibrium  $\alpha'$  martensite phase is oriented at  $45^\circ$  to prior  $\beta$  grains boundaries. The  $\beta$  phase contains a higher percentage of Vanadium (V) as compared to  $\alpha$  and  $\alpha'$  phase, which imparts higher corrosion resistance to Ti64 alloys. Figure 1.15 (b) shows the optical microstructure of SLM Ti64 alloys after heat-treatment at 1023 K for 2 hours below the  $\beta$  transus temperature of Ti64 alloys. In this,  $\alpha'$  martensite is converted into a finer lamellar mixture of  $\alpha$  and  $\beta$  within columnar prior  $\beta$  grain boundaries. Figure 1.15 (c) show the optical microstructure of SLM Ti64 alloys after heat-treatment at 1293 K for 2 hours above the  $\beta$  transus temperature of Ti64 alloys. In this,  $\alpha'$  martensite converts into completely  $\beta$  phase at high temperature. During furnace cooling,  $\beta$  phase converts partially into the  $\alpha$  phase by  $\beta$  to  $\alpha$  phase transformation. Therefore, a coarse lamellar  $\alpha + \beta$  mixture is noticed in the sample without columnar prior  $\beta$  grains [12].

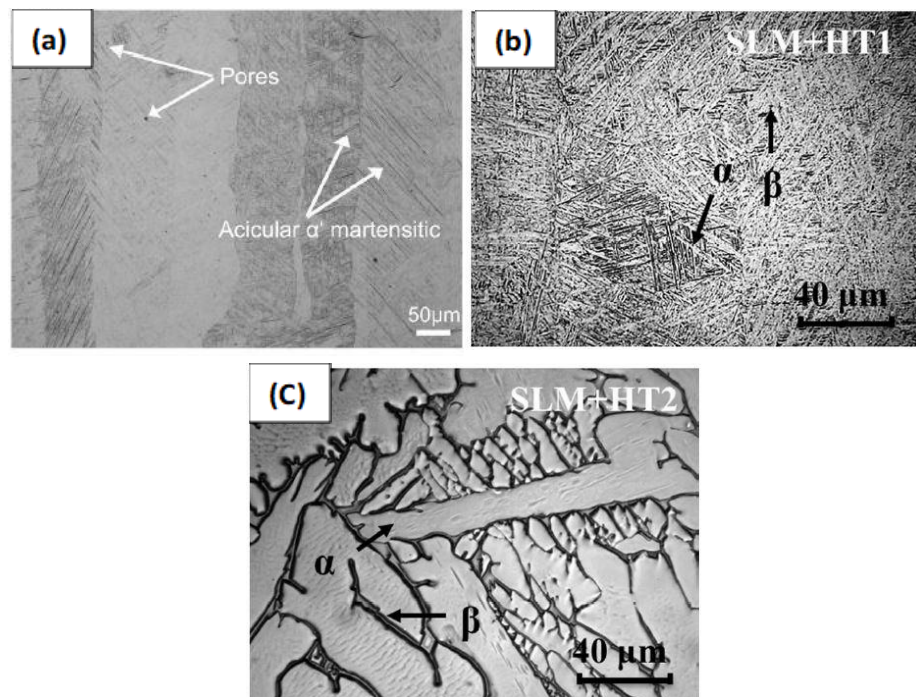
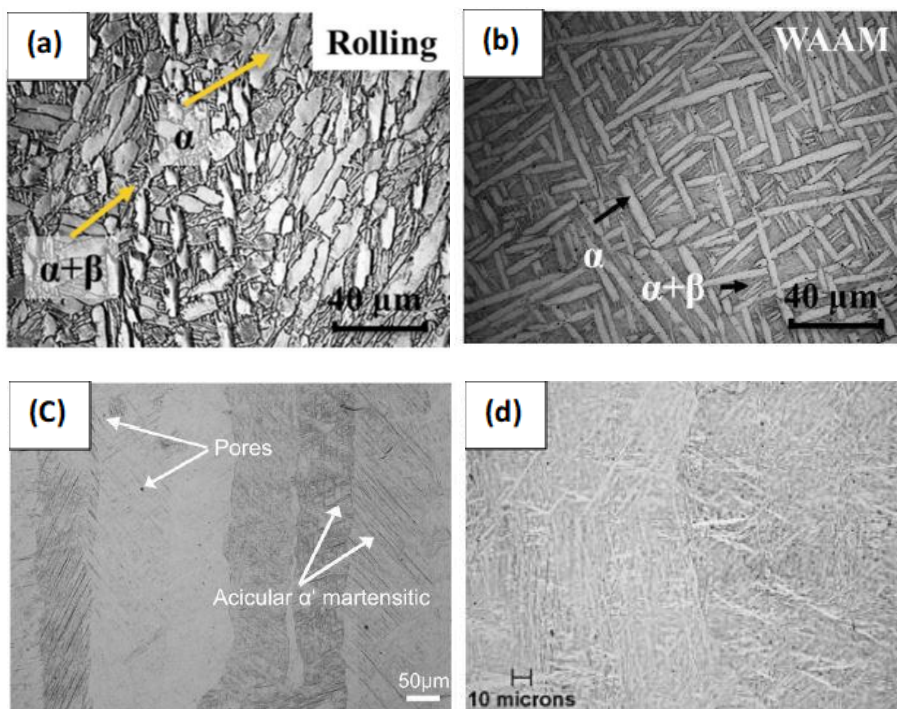


Figure 1.15 Optical microstructures of a) SLM b) SLM+HT1 c) SLM+HT2 [12]

### 1.4.6 Key microstructural differences between the Wrought and AM Ti64 alloys

Figure 1.16 (a) (b) and (c) represents the optical microstructure of rolled, WAAM, SLM and DED Ti64 alloys respectively. The rolled alloy comprises of equiaxed primary  $\alpha$  phase evenly distributed in the  $\alpha/\beta$  lamellae matrix and the WAAM comprises of fine  $\alpha$  lamellae in  $\alpha + \beta$  matrix while the SLM processed microstructure comprises of metastable or non-equilibrium acicular  $\alpha'$  martensite phase and some or a negligible amount of  $\beta$  phase. This non-equilibrium  $\alpha'$  martensite phase is oriented at  $45^\circ$  to prior  $\beta$  grains boundaries. The  $\beta$  phase contains a higher percentage of V compared to  $\alpha$  and  $\alpha'$  phase, which imparts higher corrosion resistance to Ti64 alloys. Figure 1.16 (d) shows the optical microstructure of Direct energy deposited Ti64 alloys which consists of acicular  $\alpha'$  (bright region) martensite phase within prior  $\beta$  grains (dark regions) boundaries [12].



**Figure 1.16 Optical microstructures of a) Rolled b) WAAM c) SLM d) DED [12]**

## **2. Literature Review on Corrosion Studies of Ti-6Al-4V Alloys**

### **2.1 Introduction to Corrosion**

Corrosion is the most commonly observed phenomenon in all the environments. There is a very significant loss of money associated with it because it costs in the form of failure necessitating maintenance, repairs, and replacement of damaged parts. Apart from material loss, corrosion affects the human safety, impede industrial operations, and causes danger to the environment. To overcome these detrimental effects, the adaption of timely and appropriate corrosion control is required. The definition of corrosion can be given as “*Destruction of metals and alloys in the presence of an environment by electrochemical or chemical means*” [15].

Corrosion requires five components to occur

- Anode,
- Cathode,
- Electrolyte,
- Conductor,
- Redox reactions

### **2.2 Corrosion studies on Wrought Ti-6Al-4V alloys**

Numerous studies have been published on the corrosion behaviour of the conventional manufactured Ti64 alloy.

Dalmaua *et al.* [16] compared the corrosion behaviour between rolled and sintered Ti64 alloy in phosphate buffer solution (PBS). The main objective of this study was to find out the effect of porosity and surface roughness on the corrosion resistance. They observed that sintered Ti64 (higher active surface area) alloy has more corrosion resistance than rolled (lower active surface area)Ti64 alloy due to presence of porosity and high surface roughness. The higher surface roughness increases the

active surface area for corrosion which generate higher amount of metallic cations on it but also lower passive dissolution through the oxide film, then enhancing the passive film formation.

Bahl *et al.* [17] studied influence of boron addition on the corrosion behaviour of Ti64 alloy in SBF solution. They have seen that Ti64-B alloys have higher corrosion rates as compared to Ti64 alloys. In plain Ti64 alloy, there is a micro galvanic coupling between  $\alpha$  phase and  $\beta$  phase in which  $\alpha$  phase acts as a cathode and  $\beta$  phase acts as an anode while in boron modified alloy, there is micro galvanic coupling between  $\alpha+\beta$  phase and TiB particles in which  $\alpha+\beta$  phase acts as an anode and TiB particles acts as a cathode. The  $\beta$  phase dissolves preferentially in former and  $\alpha+\beta$  phase dissolves preferentially in latter.

Alagic' *et al.* [18] have studied the corrosion behaviour of martensitic Ti64 alloy and  $\alpha+\beta$  Ti64 alloy in Ringer's solution and reported that martensitic Ti64 alloy has higher corrosion resistance than  $\alpha+\beta$  Ti64 alloy. This is due to spontaneous passivation exhibited by the martensitic Ti64 alloy leading to the formation of stable oxide protective film as compared to  $\alpha+\beta$  Ti64 alloy.

Cai *et al.* [19] have compared the corrosion behavior of different titanium alloys in modified Tani-zucchi synthetic saliva solution, were observed the influence of surface reactions on different titanium alloys. In sandblasted titanium alloys with surface reaction layer, the increasing order of corrosion rate Ti-6Al-7Nb > Ti-13Nb-13Zr > Ti-6Al-4V > CP titanium while in polished titanium alloys with surface reactions the increasing order of corrosion rate Ti-13Nb-13Zr > Ti-6Al-7Nb > Ti-6Al-4V > CP titanium, for sandblasted titanium alloys with no surface reaction the increasing order of corrosion rate as Ti-13Nb-13Zr > CP titanium > Ti-6Al-7Nb > Ti-6Al-4V.

Abdulmageed and Ibrahim [20] have performed the corrosion experiments of Ti64 alloys in 0.1M NaCl, 0.1M NaOH, 0.1M potassium hydrogen tartrate, 0.1M acetic acid, 0.04M phosphoric acid, 0.1M sodium carbonate, and 0.1M sodium oxalate reported the corrosion rate

is more in NaCl compared to the sodium carbonate and for other solutions. From various studies, it is observed that Ti64 alloys shows more corrosion resistance than the other titanium alloys.

### 2.2.1 Summary

Few important points can be summarized from the above studies

- Porosities and surface roughness have a considerable influence on the corrosion behavior.
- Increase in volume fraction of  $\beta$  phase leads to an increase in corrosion resistance.
- Addition of boron to Ti64, decreases the corrosion resistance.
- Spontaneous passivation and stable oxide film exhibit higher corrosion resistance.

## 2.2 Corrosion studies on SLM Ti-6Al-4V alloys

Limited number of corrosion studies have been published on the selective laser melting (SLM) Ti64 alloys compared to the wrought alloys.

Dai *et al.*[21] have investigated the corrosion behaviour of SLM -Ti64 alloy in 3.5 wt.% NaCl solution and have reported that commercial Ti64 alloy has more corrosion resistance as compared to SLM-Ti64 alloy. The presence of metastable acicular  $\alpha'$  phase in SLM microstructures allows the easy dissolution of alloy in solution and hence poor corrosion resistance. Further, they have also found that the volume fractions of phases influence on the corrosion behavior.

Yang *et al.*[12] have compared the corrosion behaviour among rolled, WAAM and SLM manufactured Ti64 alloy in 3.5 wt % NaCl solution. They observed that the  $\beta$  phase consists of higher percentages of V compared to  $\alpha$  and  $\alpha'$  phase. This V imparts the resistance in dissolution of  $\beta$  phase in the solution. They also provided the information of corrosion resistance of different phases based on V content and found the increasing order of corrosion resistance in phases  $\beta > \alpha > \alpha'$ .

Sui *et al.*[22] have studied the effect of build orientation on the corrosion behavior of SLM-Ti64 alloy in 3.5 wt.% NaCl solution. They built the samples oriented at 45°, 90° and 0° to the substrate and reported that in longitudinal section of 45° oriented sample to the substrate, has less corrosion resistance than the other samples. because it has lower percentages of  $\beta$  phase but in cross-section of 45° oriented sample has less corrosion resistance although it has a higher percentage of  $\beta$  phase as compared to the other samples. Therefore, this study shows that build orientation also plays a very crucial role in corrosion resistance.

### 2.2.2 Summary

Few important points can be summarized from the above studies

- The  $\beta$  phase consists of a higher percentage of vanadium that allows resistance to dissolution.
- A higher volume fraction of the  $\beta$  phase exhibits good corrosion resistance.
- Increasing order of corrosion resistance of phases  $\beta > \alpha > \alpha'$ .
- Build orientation also affects corrosion resistance.

### 2.3 Open questions

- Effect of Vanadium (V) content on the corrosion resistance.
- Role of the  $\beta$  phase on the corrosion resistance.
- Effect of SLM parameters such as build orientation, laser scan rotation, etc.
- Role of microstructure on the corrosion behavior has to be ascertained.
- What is the influence of metastable  $\alpha'$  phase and prior  $\beta$  grains need to be investigated?
- Role of crystallographic texture generated during additive manufactured method also may influence the corrosion behavior which needs to be understood.

### **3. Objective of Work**

1. To conduct corrosion experiments on the SLM Ti-6Al-4V alloys to understand
  - 1.1 Influence of meso or micro-structure
  - 1.2 Metastable  $\alpha'$  phase and prior  $\beta$  grains
2. To simulate the corrosion behaviour using COMSOL Multiphysics software
3. To compare the experimental results with simulation results
4. To analyze the mesh sensitivity effect

## **4. Materials and Experiments**

In this chapter, the materials and experimental techniques used in the current study are described in detail.

### **4.1. Materials used in the current study**

The materials used in the experiments are manufactured using selective laser melting (SLM) technique. The coupons are prepared with ELI grade Ti-6Al-4V powder in an argon gas environment in SLM unit equipped with a Yb:YAG fiber laser. The coupons are fabricated with different combinations of processing parameters: laser power 280-Watt and 320-Watt, scan speed 1200 mm/s and 1250 mm/s, and scan spacing 0.14 mm and 0.12 mm respectively for the layer thickness of 30  $\mu\text{m}$  and 60  $\mu\text{m}$  with scan rotation of  $67^\circ$ . Once all the coupons were fabricated, they are annealed at  $650^\circ\text{C}$  for 3h to relieve the internal thermal stresses generated due to high cooling rates. The purpose of rotating the scan direction between two successive layers is to provide some degree of isotropy to the sample and reduce porosity [23][24]. The  $67^\circ$  scan rotation used for ensuring the highest number of scan rotations between the laser tracks with similar orientation [14]. In this study, it is vital to examine the effect of layer thickness, scan spacing, laser power, and laser scan speed on the corrosion resistance of SLM-manufactured samples. Moreover, for investigating the effect of build planes and scan planes on the corrosion resistance. Thin plates of 3cm X 3cm X 5mm are cut from these large coupons along the two principal directions namely the build direction (B) and the scan direction (S). Four different types of samples are used in the current study namely B3067, S3067, B6067, and S6067.

### **4.2 Experiments**

#### **4.2.1 Microscopic examination**

The samples are then taken for microstructural examination by following standard metallographic procedure. First the samples are hot mounted using SimpliMet3000 mounting press of Buehlermake. The four samples

are placed on the mounting mold completely covered with Pheno cure powder having a phenolic thermosetting resin. Under the action of high temperature and pressure, the resin melts inside molds and covers the specimen, subsequently on cooling the resin sets and becomes hard. After that samples polished using an EcoMet polishing machine of Buehler make. The samples are polished with emery papers with the starting grit size of 80, then on 240,320, 400, 600, 800, 1000, 1500, 2500, and 4000 for 10 minutes each. A steady supply of water is always maintained while polishing and the sample is also held in a fixed position so that all the scratched are in one direction. When the next size grit size emery paper is taken for polishing the sample should be held in such a way that the direction of material removal is perpendicular to the direction of lay. Final polishing is done with 3  $\mu\text{m}$  alumina paste over the velvet cloth until the mirror finish is obtained. The polished specimen is cleaned ultrasonically first with ethanol and then with distilled water for 5 minutes each and finally, air-dried using the blower. After metallographic preparation, the microstructural examination was conducted by etching the surface of the sample with a suitable etchant. Etching preferentially oxidizes all the boundaries like grain, colony, and lath boundaries, thus other matrix gets highlighted which can be observed under an inverted optical microscope. The etchant used for Ti64 alloy is Kroll's reagent having a composition of 10% HF, 15% HNO<sub>3</sub>, and 75% distilled water by volume. The etching is done by swabbing the polished face of the specimen for approximately 2.5 to 4 minutes using a cotton swab followed by washing it by tap water and drying the etched surface with a hot blower.

#### **4.2.2. Electrochemical Measurements**

The sample size of 2.25 cm<sup>2</sup> surface area with 1 mm thickness is ground up to 2500 grit emery papers and subsequently polished with alumina. Finally, all the samples are ultrasonically cleaned in ethanol, dried, and ready for an electrochemical test. Only a 1cm<sup>2</sup> surface area is considered as a working electrode. The electrochemical tests are performed in 0.61M (3.5 wt.%) NaCl solution at room temperature by using a NOVA

AutoLab in a three-electrode cell system. In which platinum wire is used as a counter electrode and Ag/AgCl (1M saturated KCl) is used as a reference electrode.

### 4.2.3 Corrosion Rate Calculation

Corrosion rate (CR) in this work has been calculated from the ASTM standard G 102-89 [26],

According to the formula

$$\text{Corrosion rate (CR)} = K \frac{i_{\text{corr}}}{\rho} \text{EW} \quad (1)$$

Where  $K=3.27\text{E-}3 \text{ mm g } \mu\text{A}^{-1} \text{ cm}^{-1} \text{ yr}^{-1}$

$i_{\text{corr}}$  = Corrosion current density ( $\mu\text{A cm}^{-2}$ )

$$\text{Equivalent weight (EW)} = \frac{1}{\sum \frac{f_i n_i}{M_i}} \quad (2)$$

Where  $f_i$  = Mass fraction of  $i^{\text{th}}$  element in alloy

$n_i$  = Valency of  $i^{\text{th}}$  element in alloy

$M_i$  = Atomic weight of  $i^{\text{th}}$  element in alloy

The density of Ti64 ( $\rho$ ) =  $4.43 \text{ g/cm}^3$

Table 2 contains the very useful data required for the calculation of equivalent weight for Ti64 alloys. The obtained value of equivalent weight for Ti64 alloys after the calculation is 11.88

**Table 2.** Calculation of Equivalent Weight (EW)

Element	Mass fraction ( $f_i$ )	Valency ( $n_i$ )	Atomic weight ( $M_i$ ) (g/mol)
Ti	0.9	4	47.9
Al	0.06	3	26.98
V	0.04	3	50.94

## 5. Modelling Methodology

In this chapter, the governing equation and boundary conditions used for corrosion simulation in the current study are described in detail.

### 5.1 Governing Equation

Mass transport of chemical species  $i$  occur due to diffusion mechanism, electromigration mechanism, and convection mechanisms. Therefore, after considering all the above mechanisms Nernst - Planck equation [27][28] represents as,

$$\mathbf{N}_i = -D_i \nabla C_i - Z_i u_{m,i} C_i F \nabla \Phi_l + C_i \mathbf{u} \quad (3)$$

Where,  $\mathbf{N}_i$ (vector) is the flux of species  $i$ ,  $C_i$ (Scalar) represents the concentration of the species  $i$ ,  $Z_i$  its valence,  $D_i$ (Tensor) its diffusivity,  $F$  denotes the Faraday constant,  $\Phi_l$ (Scalar) is the electrolyte potential,  $\mathbf{u}$  the velocity vector,  $u_{m,i}$ (Tensor) =  $\frac{D_i}{RT}$  (electrical mobility of species)

In Eq. (3), the flux of species  $i$  involves three mechanisms of transport, the left-most term is diffusion mechanism, the rightmost term is convection mechanism and the middle one is electromigration (migration) mechanism.

The diffusion mechanism causes movement of ions from regions of higher to lower concentrations. The electromigration mechanism, anions, and cations move parallel and anti-parallel to the direction of the electric field. The convection mechanism can be natural convection or forced convection. Natural convection occurs due to the density differences between the electrolyte near the anode or cathode and bulk electrolyte. Forced convection also occurs due to the same mechanism except the velocity field provided to the electrolyte by some kind of external means.

Therefore, the net current flow in the electrolyte is given by-

$$\mathbf{i}_l = F \sum Z_i \mathbf{N}_i \quad (4)$$

On putting the value of  $\mathbf{N}_i$  in the above equation

$$\mathbf{i}_l = -F \sum Z_i D_i \nabla C_i - \frac{F^2}{RT} \nabla \Phi_l \sum Z_i^2 C_i D_i + \mathbf{u} \sum Z_i C_i \quad (5)$$

Eq. (5) is used for the **Tertiary current distribution** interface.

Assumptions involved in the current study-

1. The electrolyte solution is thoroughly mixed as a result concentration gradients are negligible.
2. The solution is electroneutral that leads to negligible convection.
3. Oxidation reactions, as well as reduction reactions, were taking place only on the working electrode.
4. Initial electrolyte potential is taken as zero.

Current flow in the electrolyte will be purely based on migration (For primary and secondary current distribution interface)

Therefore, current flow in the electrolyte can be given as-

$$\mathbf{i}_l = -\frac{F^2}{RT} \nabla \Phi_l \sum Z_i^2 C_i D_i \quad (6)$$

From the above equation, we can find electrolyte conductivity (tensor quantity).

$$\sigma_l = \frac{F^2}{RT} \sum Z_i^2 C_i D_i \quad (7)$$

Hence,

$$\mathbf{i}_l = -\sigma_l \nabla \Phi_l \quad (8)$$

Eq. (8) is used for the **Primary** as well as **Secondary current distribution** interface.

The primary current distribution interface is used for estimation of ohmic losses occurred due to ionic flow and electronic flow through the electrode and electrolyte respectively. The secondary current distribution interface is somehow similar to the primary current distribution interface only difference, it considers the activation

overpotential or kinetics at the electrodes. Tertiary current distribution interface considers the transport of charges (ions) within the electrolyte along with kinetics at the electrodes.

## 5.2 Geometry and Boundary Conditions

Figure 5.1 illustrates 2D meshed geometry used for simulations of all the samples which consists of electrolyte domain of width 1cm, working electrode is at the extreme left edge of length 1 cm, and the correspondingly counter electrode is at the extreme right edge of length 1 cm, Table 3 contains the input parameters used for simulations. For corrosion analysis, a half-cell reaction model is developed. in which the redox reactions take place on the anode or working electrode and counter electrode kinetics can be neglected. A 2D geometry is used for reducing complexity. A default coarse triangular mesh element was used in the analysis because of reducing the convergence problems while solving the stationary study. Mesh sensitivity studies have been conducted to optimize the mesh size that gives results with lesser computational time. The Butler-Volmer equation is used as a boundary condition for working electrode and the electrolyte potential was set to zero, is used as a boundary condition for counter electrode and insulation boundary condition is applied for all the other boundaries of the electrolyte domain.

Butler-Volmer equation is used for the reversible process in which either anodic or cathodic current may flow rely on the sign and magnitude of the polarization.

$$i_{\text{net}} = i_{\text{corr}} \left( \exp\left(\frac{\alpha_a F \eta}{RT}\right) - \exp\left(\frac{-\alpha_c F \eta}{RT}\right) \right) \quad (9)$$

Where,  $i_{\text{net}}$  is a net current density,  $i_{\text{corr}}$  is corrosion current density,  $F$  is faraday's constant,  $R$  is a gas constant,  $\alpha_a$  is anodic transfer coefficient,  $\alpha_c$  is cathodic transfer coefficient,  $\eta$  is overpotential,  $T$  is temperature.

Electrolyte potential used for making the half- cell reaction model, is taken as zero.

$$\Phi_{\text{bnd}} = 0 \quad (10)$$

Where,  $\Phi_{\text{bnd}}$  is boundary electrolyte potential.

Insulation boundary condition defines the boundaries of the cell that do not face the conductor, can be given as

$$\mathbf{i}_l \cdot \mathbf{n} = 0 \quad (11)$$

Where,  $\mathbf{i}_l$  is an electrolyte current density vector,  $\mathbf{n}$  is a normal vector.

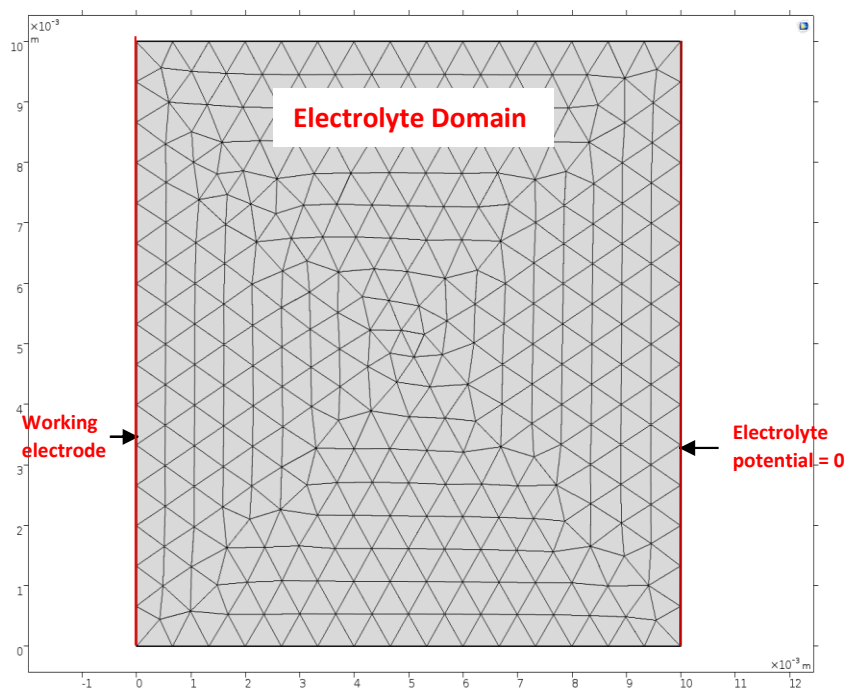


**Figure 5.1 Schematic of 2D meshed geometry in COMSOL Multi-physics**

**Table 3.** Input parameters required for corrosion simulation of SLM manufactured Ti-6Al-4V alloy

<b>Property</b>	<b>Values</b>	<b>Units</b>
$\sigma$ conductivity of the electrolyte	1.09	S/m
Working electrode length	0.01	m
Counter electrode length	0.01	m
The thickness of the electrolyte domain	0.01	m
Corrosion potential ( $E_{\text{corr}}$ ) for B3067	-0.1745	V vs Ag/AgCl
Corrosion current density ( $i_{\text{corr}}$ ) for B3067	6.58E-3	A/m <sup>2</sup>
Corrosion potential ( $E_{\text{corr}}$ ) for S3067	-0.2155	V vs Ag/AgCl
Corrosion current density ( $i_{\text{corr}}$ ) for S3067	4.66E-3	A/m <sup>2</sup>
Corrosion potential ( $E_{\text{corr}}$ ) for B6067	-0.3819	V vs Ag/AgCl
Corrosion current density ( $i_{\text{corr}}$ ) for B6067	1.06E-4	A/m <sup>2</sup>
Corrosion potential ( $E_{\text{corr}}$ ) for S6067	-0.1161	V vs Ag/AgCl
Corrosion current density ( $i_{\text{corr}}$ ) for S6067	3.71E-4	A/m <sup>2</sup>
Anodic transfer coefficient	0.5	1
Cathodic transfer coefficient	0.5	1

## 6. Results and Discussions

### 6.1 Microstructure and features

Microstructure shows grain structures and phases present in various samples. In the SLM process, the rapid heating and cooling leads to the formation of fine and acicular  $\alpha'/\alpha$  laths. These laths are oriented at  $45^\circ$  to the prior  $\beta$  grain boundaries [29][30]. Both  $\alpha'$  and  $\alpha$  phases have HCP crystal structure but having different c/a ratios,  $\alpha'$  phase has a c/a ratio 1.589 while  $\alpha$  phase has 1.59-1.6 [31]. The non-equilibrium  $\alpha'$  phase is more prone to corrosion due to being in a higher energy state [21]. The  $\beta$  phase contains more percentages of vanadium (V) content. This V imparts the resistance in the dissolution of the  $\beta$  phase in the solution.  $\beta$  phase has higher corrosion resistance than  $\alpha'$  phase and  $\alpha$  phase while  $\alpha'$  phase has lowest corrosion resistance with the corrosion resistance of  $\alpha$  phase lying in between these two phases [12]. For combinations of thickness layer 30  $\mu\text{m}$  and 60  $\mu\text{m}$  with scan rotation  $67^\circ$ , the melt pool does not overlap with the next layer due to the  $67^\circ$  scan rotation, as a result, irregular arrangement of the prior  $\beta$  grain boundaries. In B-plane of the sample 3067 (Figure 6.1 (a)), prior  $\beta$  grains appear equiaxed with an average grain diameter of 140  $\mu\text{m}$  that is equal to scan spacing employed during SLM. However, in S-plane of sample 3067 (Figure 6.1 (b)), prior  $\beta$  grains appear as columnar with walls of these grains are jagged and discontinuous. In the B-plane of the sample 6067 (Figure 6.1 (c)), prior  $\beta$  grains appear as equiaxed. Whereas, in S-plane of the sample 6067 (Figure 6.1 (d)), prior  $\beta$  grains boundaries appear short and irregular. Both B and S-planes show this type of morphologies due to the mismatch in the laser tracks.

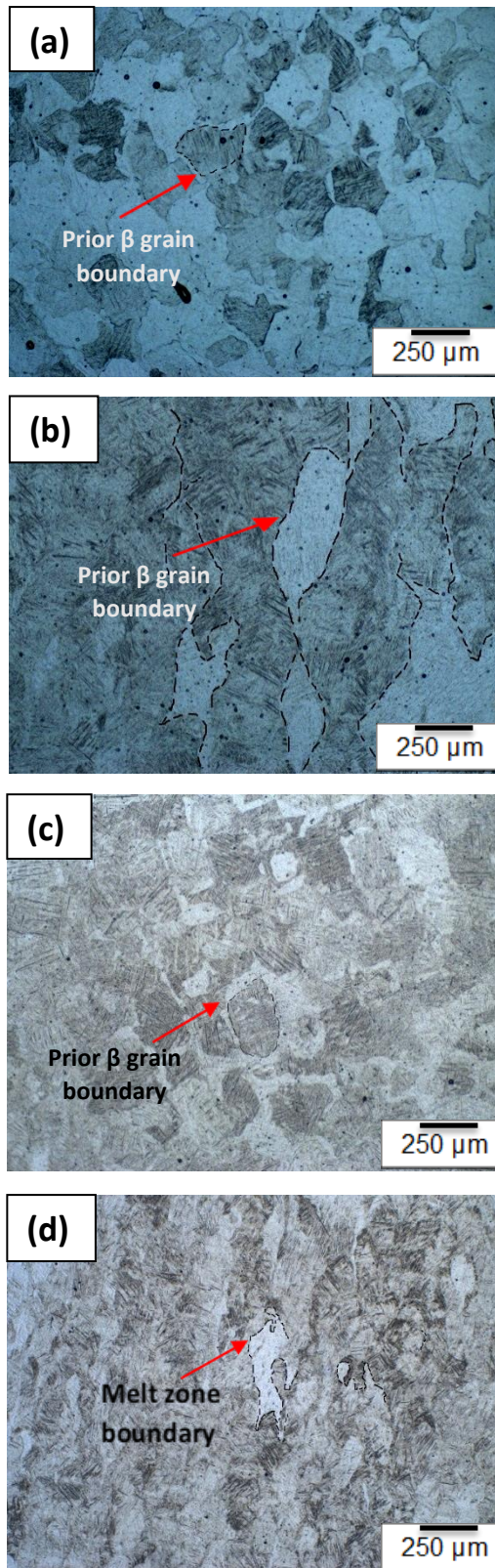
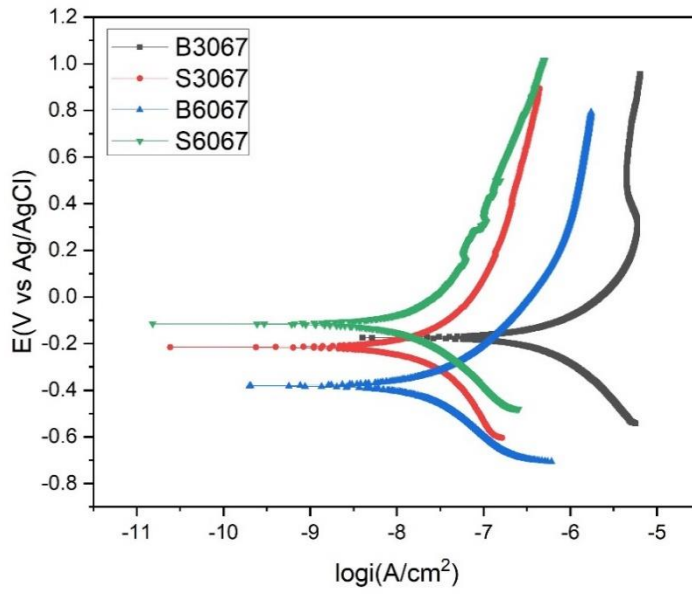


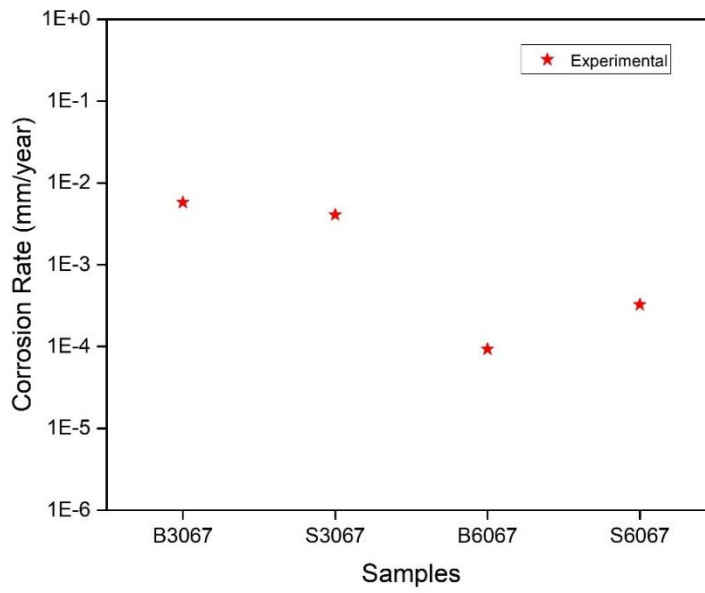
**Figure 6.1** Optical microstructures of a) B3067, b) S3067, c) B6067, d) S6067. Dashed lines in (a) , (b), (c), and (d) are merely for ‘guiding the eye’

## 6.2 Tafel and other relevant plots and their description

Potentiodynamic polarization calculation belongs to the most commonly used direct current (DC) electrochemical technique in corrosion measurement. In this, a wide range of potential is applied on the working electrode because of which, the metal surface oxidizes or reduces due to oxidation or reduction reactions occurs, and as a result of which, sufficient current is generated. The presentation of the potential in the function of current density  $\log i$  or  $i$  for each measured point results in obtaining the polarization curve. The polarization curve consists of anodic polarization curve and cathodic polarization curve. The polarization curve can be used to estimate the corrosion rate and corrosion potential of the metal in the given environment by drawing the tangent to each polarization curve. These tangents (Tafel slope) intersect corresponding to electrode potential then that point indicates the corrosion current density in  $\log i$  or  $i$  axis. In this study, Figure 6.2 (a) shows the potentiodynamic polarization curves of the samples in 3.5 wt.% NaCl solution. It took sufficient time to get a stable open circuit potential (OCP) before polarization tests. Moreover, It is very crucial to judge the ability of corrosion resistance by using corrosion parameters in the polarization curve such as corrosion potential ( $E_{\text{corr}}$ ) and corrosion current density ( $i_{\text{corr}}$ ) and corrosion rate (CR). The data of corrosion parameters are shown in Table 5. The  $i_{\text{corr}}$  of the sample B6067 is lowest than other samples which means it exhibits the best corrosion resistance while the  $i_{\text{corr}}$  of sample B3067 is highest than other samples which means it exhibits worst corrosion resistance and remaining samples exhibit corrosion resistance in between sample B6067 and sample B3067. Figure 6.2 (b) shows the comparison in the corrosion rate obtained from the ASTM standard formula for samples used in this study.



(a)

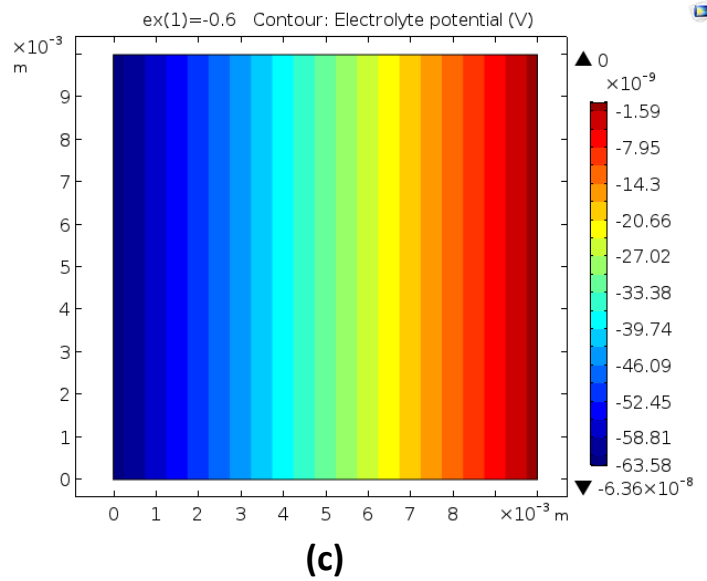
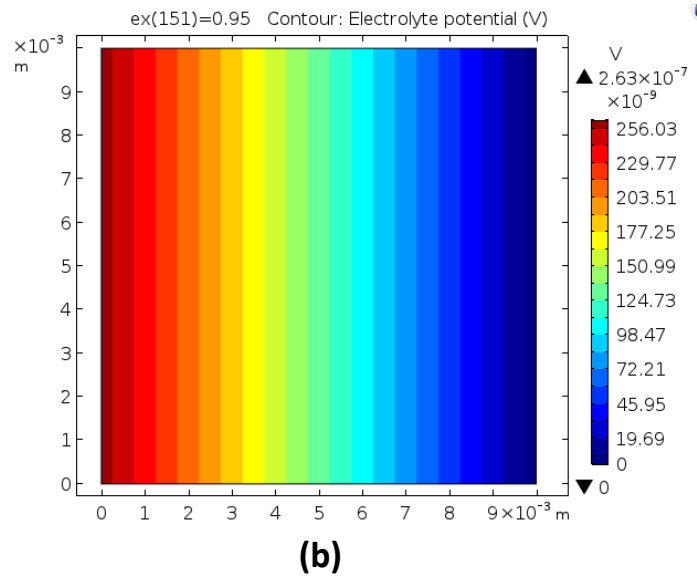
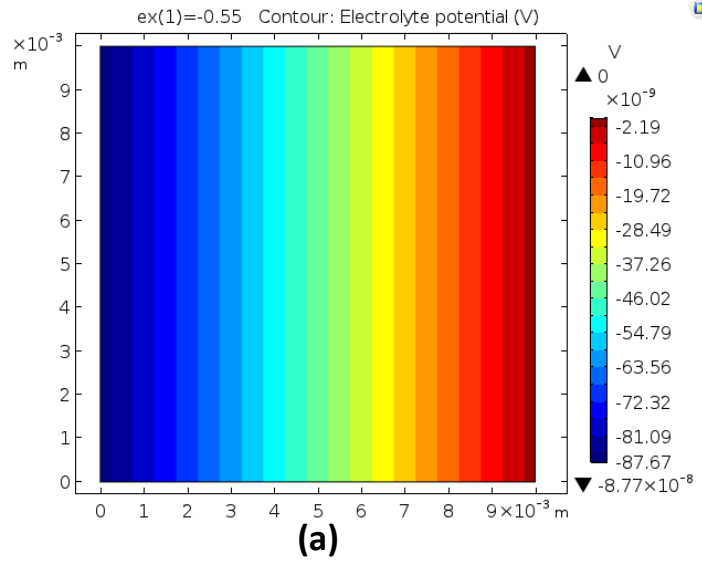


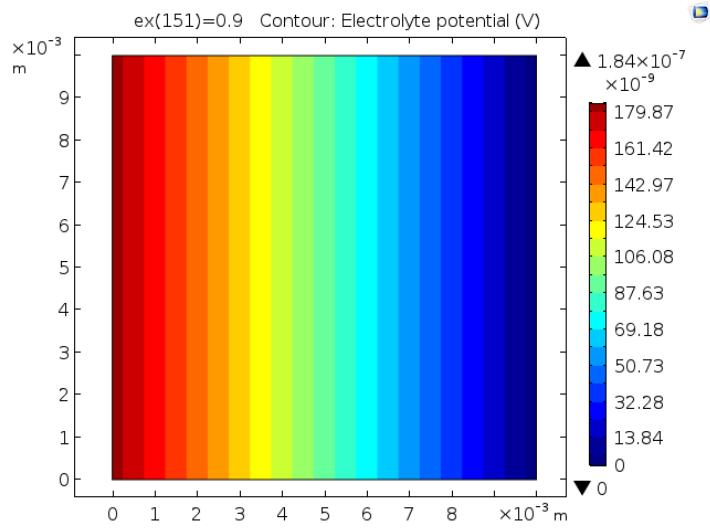
(b)

**Figure 6.2 Potentiodynamic polarization curve for SLM manufactured Ti-6Al-4V alloys (a) Corrosion rate comparison (b)**

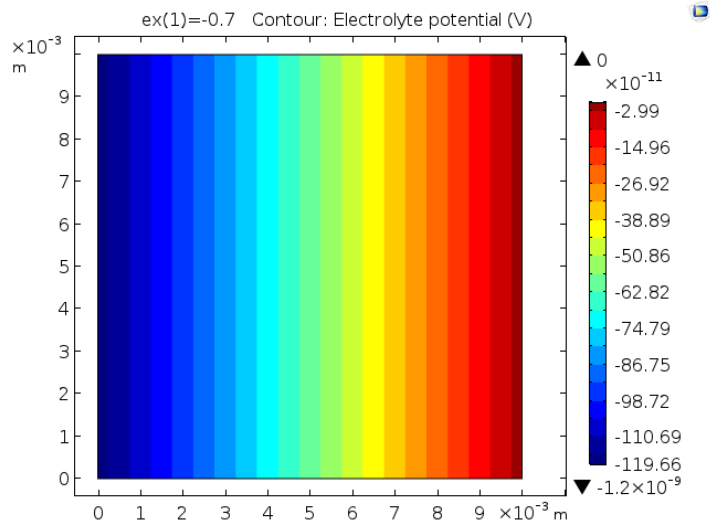
### **6.3 Electrolyte potential obtained from corrosion simulation**

Electrolyte potential indicates the potential generated due to the ions within the electrolyte. It is also one of the important parameters for predicting the corrosion behavior of samples. The electrolyte contains various ions such as  $\text{Ti}^{4+}$ ,  $\text{Na}^+$ ,  $\text{Cl}^-$  etc. These ions are the main reason for generating the electrolyte potential. Figure 6.3 shows the contour graphs of the electrolyte potential of various samples that are the cumulative potential of  $\text{Ti}^{4+}$ ,  $\text{Na}^+$ ,  $\text{Cl}^-$  etc. ions. These graphs are at extreme potential applied i.e. from negative to the positive potential applied. At negative potential applied, samples exhibit negative electrolyte potential while at positive potential applied, samples exhibit positive electrolyte potential. Moreover, the values of these potential generated are very small i.e. in the order of  $10^{-7}$  to  $10^{-9}$  V. The electrolyte potential is maximum near to the working electrode because there is the density of ions are higher as compared to other locations and varying along the electrolyte domain length due to variation in ions density but zero where we applied the electrolyte potential equals to zero boundary condition. If electrolyte potential is higher means, the sample has less corrosion resistance and vice-versa. In this study, the electrolyte potential of sample B6067 is lowest than other samples which means it exhibits the best corrosion resistance while the electrolyte potential of sample B3067 is highest than other samples which means it exhibits worst corrosion resistance and other samples exhibit corrosion resistance in between sample B6067 and sample B3067.

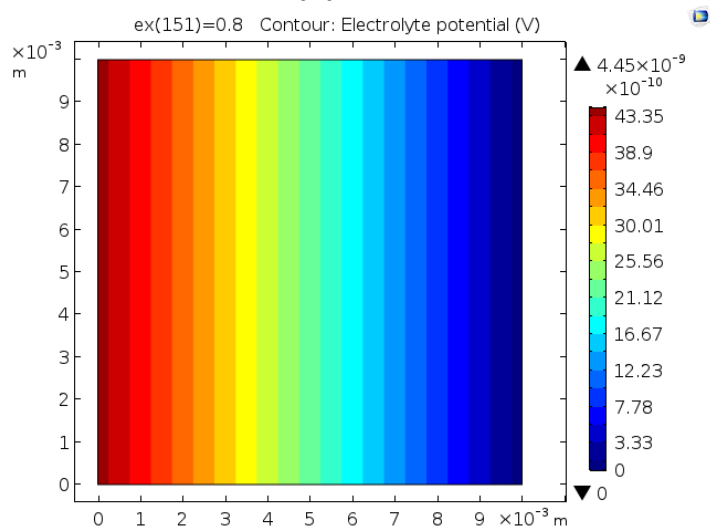




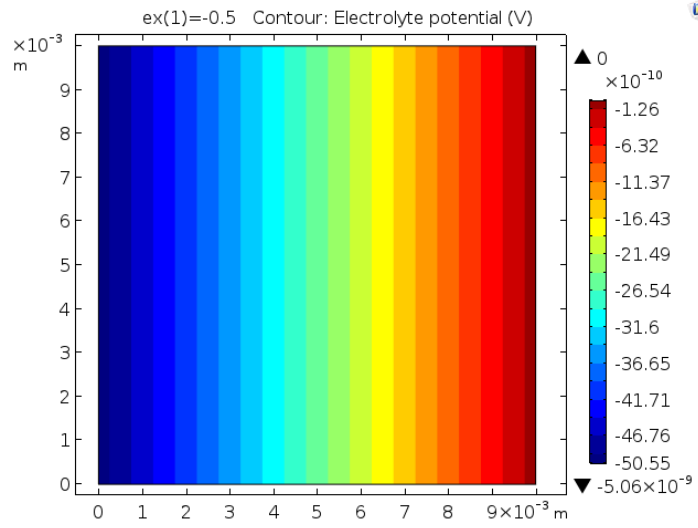
(d)



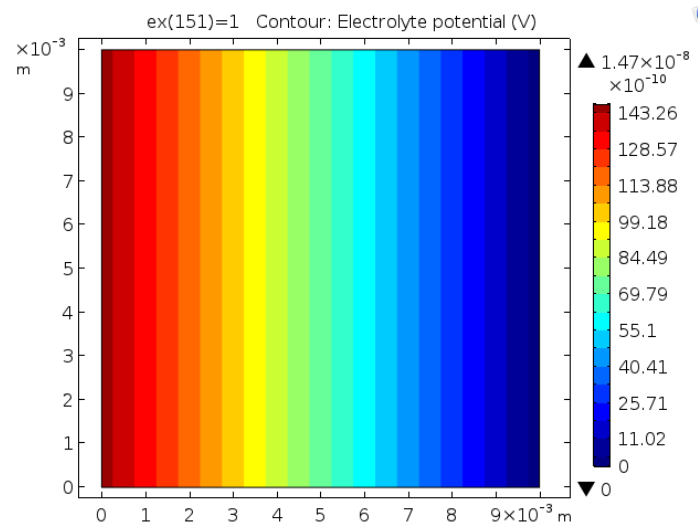
(e)



(f)



(g)

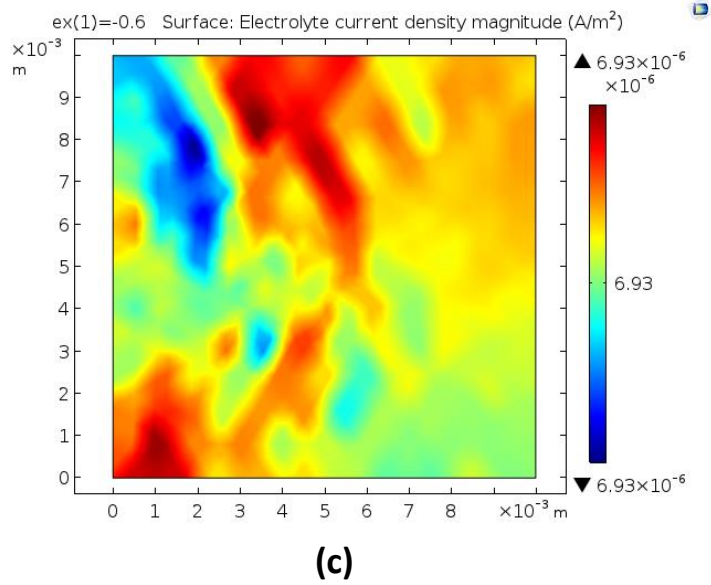
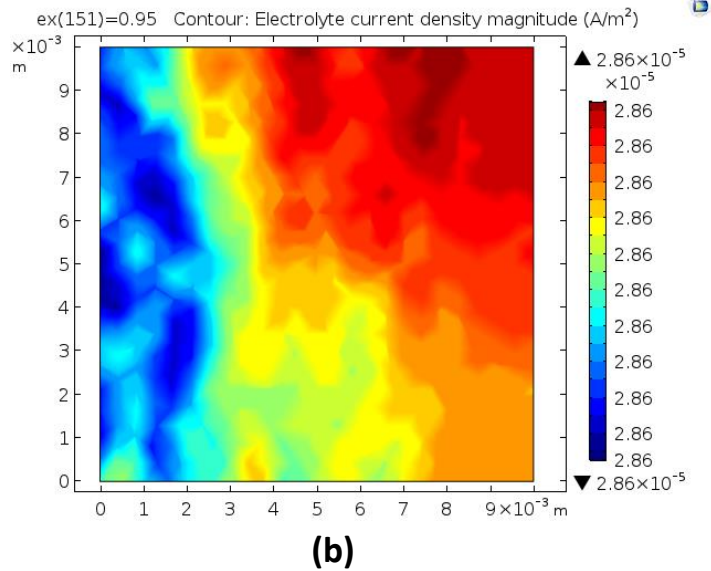
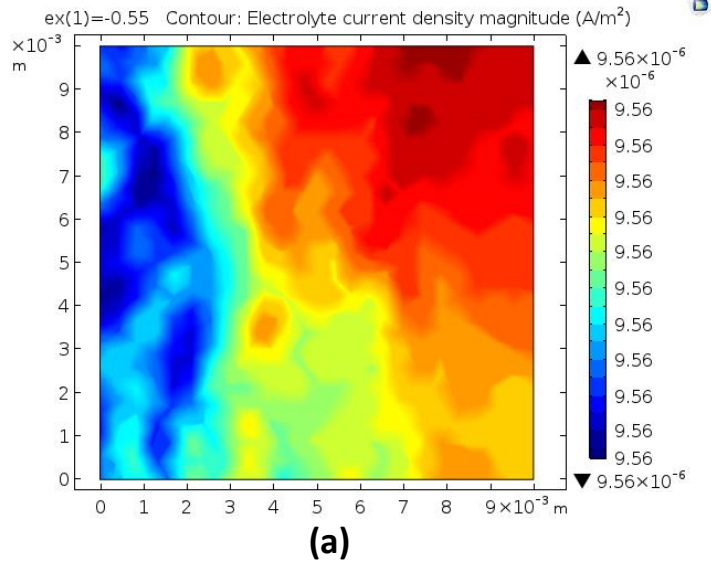


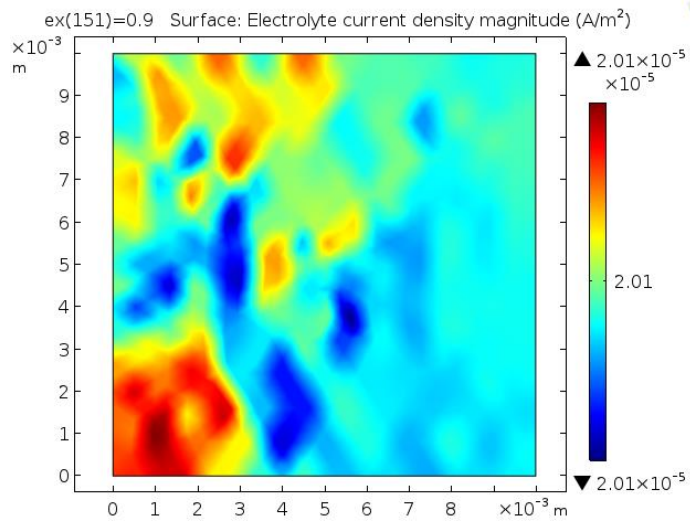
(h)

**Figure 6.3 Electrolyte potential of samples at two extreme values of applied voltage (a, b) B3067, (c,d) S3067, (e,f) B6067, (g,h) S6067**

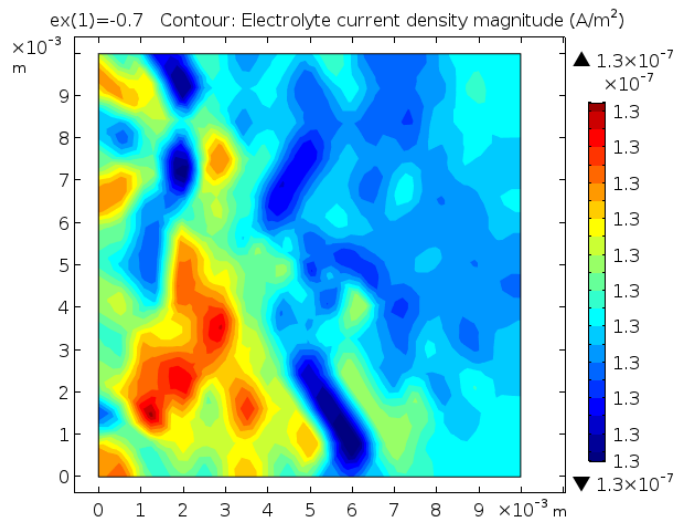
## 6.4 Electrolyte current density obtained from corrosion simulation

Electrolyte current density indicates the current generated due to the movement of ions within the electrolyte. It is also one of the important parameters for predicting the corrosion behaviour of samples. This electrolyte contains various ions such as  $Ti^{4+}$ ,  $Na^+$ ,  $Cl^-$  etc. These ions are the main reason for generating electrolyte current density. Fig. 6.4 shows the contour graphs of electrolyte current density magnitude of various samples that are the cumulative current density generated due to movements of  $Ti^{4+}$ ,  $Na^+$ ,  $Cl^-$  etc. ions. These graphs are at extreme potential applied i.e. from negative to the positive potential applied. At negative potential applied, samples exhibit less electrolyte current density magnitude while at positive potential applied, samples exhibit higher electrolyte current density magnitude. Moreover, the values of these current density generated are very small i.e. in the order of  $10^{-5}$  to  $10^{-7}$  A/m<sup>2</sup>. The electrolyte current density is the same along the electrolyte domain length due to the magnitude of it. If electrolyte current density is higher means, the sample has less corrosion resistance and vice-versa. In this study, electrolyte current density of sample B6067 is lowest than other samples which means it exhibits the best corrosion resistance while the electrolyte current density of sample B3067 is highest than other samples which means it exhibits worst corrosion resistance and remaining samples exhibit corrosion resistance in between sample B6067 and sample B3067.

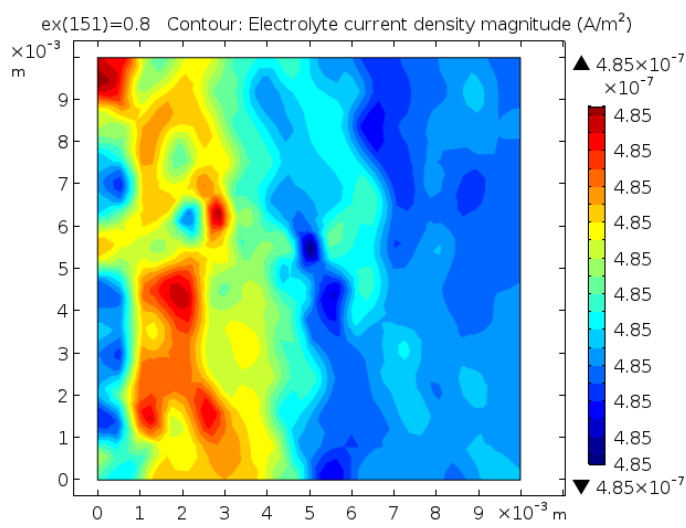




(d)



(e)



(f)

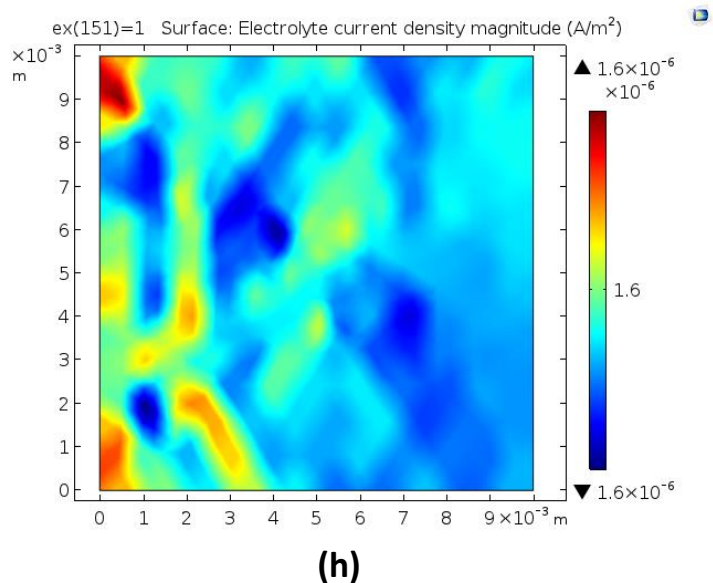
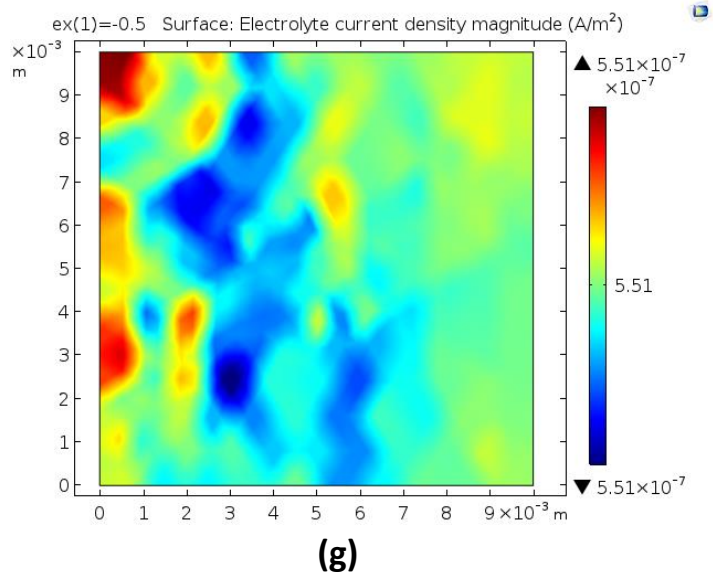


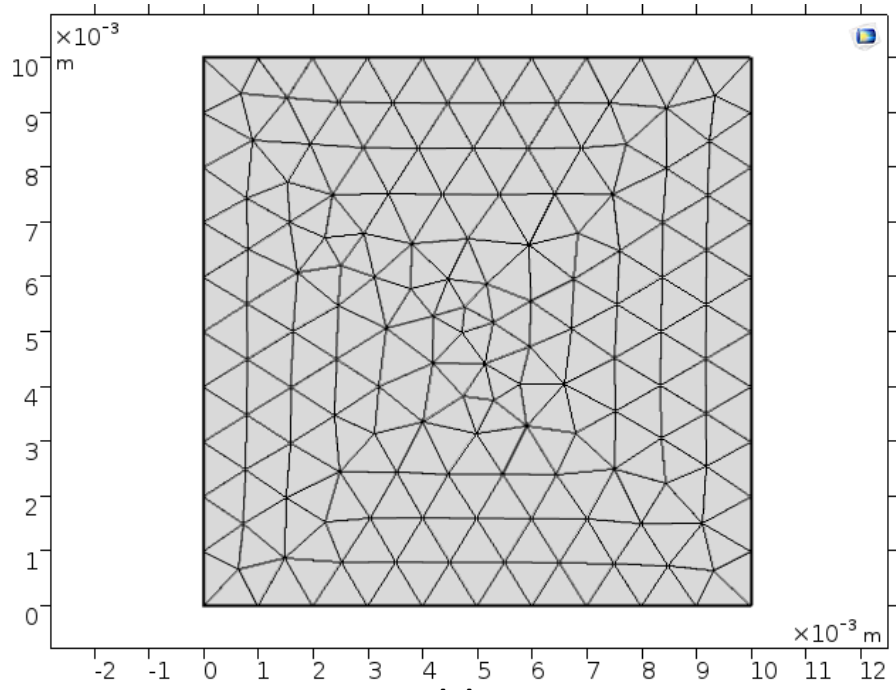
**Figure 6.4 Electrolyte current density for samples at two extreme values of applied voltage (a, b) B3067, (c, d) S3067, (e, f) B6067, (g, h) S6067**

## 6.5 Mesh sensitivity results

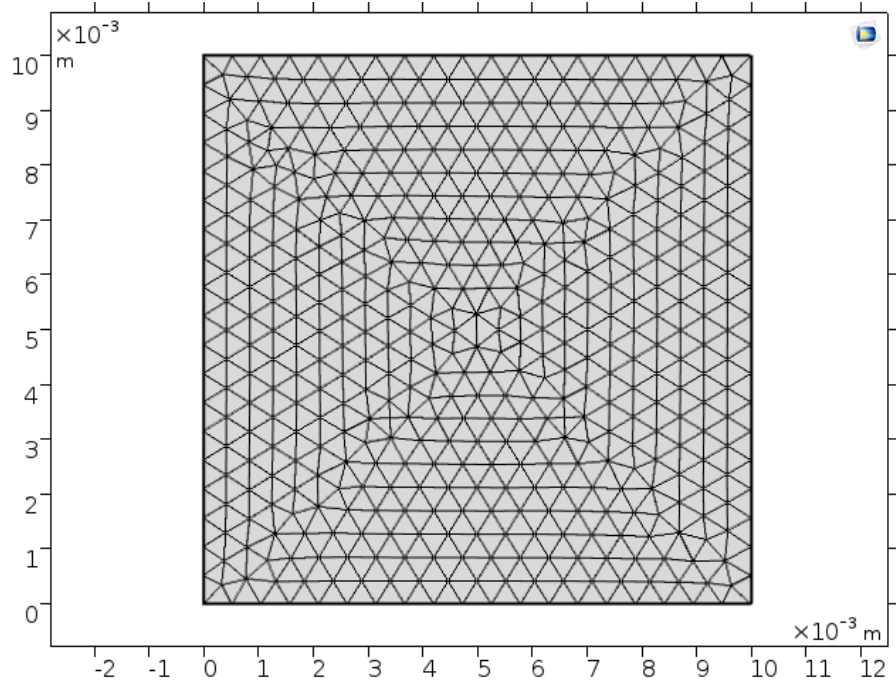
The objective of this study is to analyze the effect of mesh sensitivity on the corrosion rate, current density, and corrosion potential obtained from two-dimensional corrosion modeling. Basically, in this study, we saw the effect of coarser mesh as well as finer mesh on the corrosion parameters and also on the polarization curve. In coarser mesh analysis, there were 268 domain elements and 40 boundary elements. The domain elements are those elements which are consisted of triangular elements in the electrolyte domain and boundary elements consisted of triangular elements on the boundaries. In finer mesh analysis, there were 928 domain elements and 76 boundary elements. The table 4 shows the computation time taken for the corrosion simulation for coarse mesh and fine mesh and conclude that coarser mesh was taking less computing time as compared to finer mesh due to fewer elements. The polarization curves obtained after adapting the coarser mesh and finer mesh, are overlapping to each other for all the samples. The main reason behind this is two-dimensional modeling. Actually, in two-dimensional modeling, we assumed one edge as a working electrode (Figure 5.1) due to this, edge is not affected by coarser or finer mesh.

**Table 4.** Computation time taken by coarser mesh and finer mesh

<b>Sample</b>	<b>Coarser Mesh</b>	<b>Finer Mesh</b>
B3067	6 min.19 sec	14 min.53 sec
S3067	7 min. 58 sec	12 min.11 sec
B6067	6 min. 3 sec	12 min.17 sec
S6067	5 min.26 sec	12 min. 36 sec



(a)



(b)

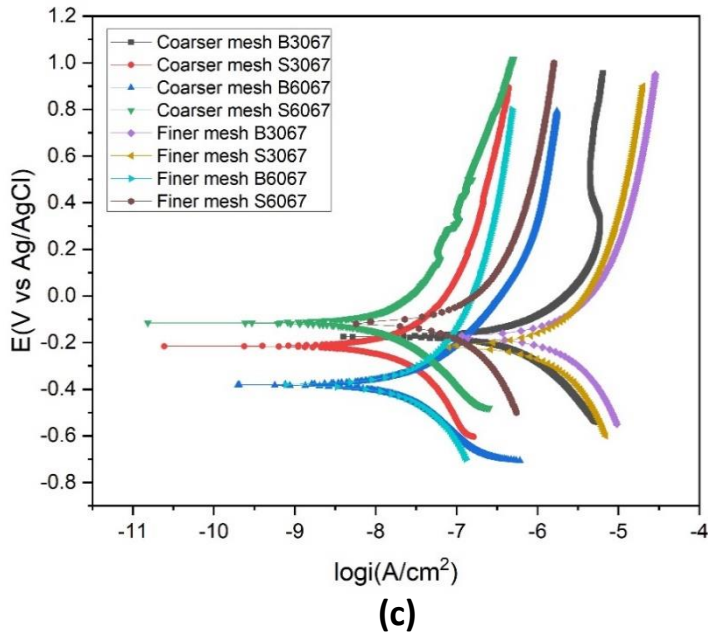


**Figure 6.5 Schematic of 2D geometry with a) Coarser mesh b) Finer mesh c) comparison in polarization curve**

**Table 5.** Summary of corrosion current density and corrosion rate for SLM Ti-6Al-4V alloy in this study.

Sample	Experimentally Corrosion current density ( $i_{\text{corr}}$ ) (A/cm <sup>2</sup> )	Experimentally Corrosion rate (C.R) (mm/yr.)	Simulated Corrosion current density ( $i_{\text{corr}}$ ) (A/cm <sup>2</sup> )	Simulated Corrosion rate (C.R) (mm/yr.)
B3067	6.58E-7	5.77E-3	2.01E-6	1.77E-2
S3067	4.66E-7	4.10E-3	1.09E-6	9.56E-3
B6067	1.06E-8	9.30E-5	2.41E-8	2.11E-4
S6067	3.71E-8	3.26E-4	1.24E-7	1.10E-3

## 6.6 Comparison of experiment and simulation results

The objective of this study is to compare the experimental polarization curve and simulated polarization curve results. The electrochemical parameters collected through experimental data such as corrosion potential ( $E_{\text{corr}}$ ) and corrosion current density ( $i_{\text{corr}}$ ), were used into COMSOL Multiphysics for validation. Figure 6.6 (a) shows the polarization curves obtained from corrosion simulation and potentiodynamic polarization tests. The simulated polarization curves exhibit the same trend as the experimental polarization curve. The  $i_{\text{corr}}$  obtained from simulation for sample B6067 is lowest than other samples which means it exhibits the best corrosion resistance while the  $i_{\text{corr}}$  sample B3067 is highest than other samples which means it exhibits worst corrosion resistance and remaining samples exhibit corrosion resistance in between sample B6067 and sample B3067. Moreover, Figure 6.6 (b) shows the simulated corrosion rate is much higher than that of the experimental corrosion rate. The reason behind this is the consideration of some assumptions during the simulation. The data of corrosion parameters obtained from the simulation are enlisted in Table 5. The corrosion rate calculated from the simulation for samples B3067, S3067, B6067, and S6067 is 3.05 times, 2.33 times, 2.26 times, and 3.37 times higher than that of experimentally calculated corrosion rate respectively.

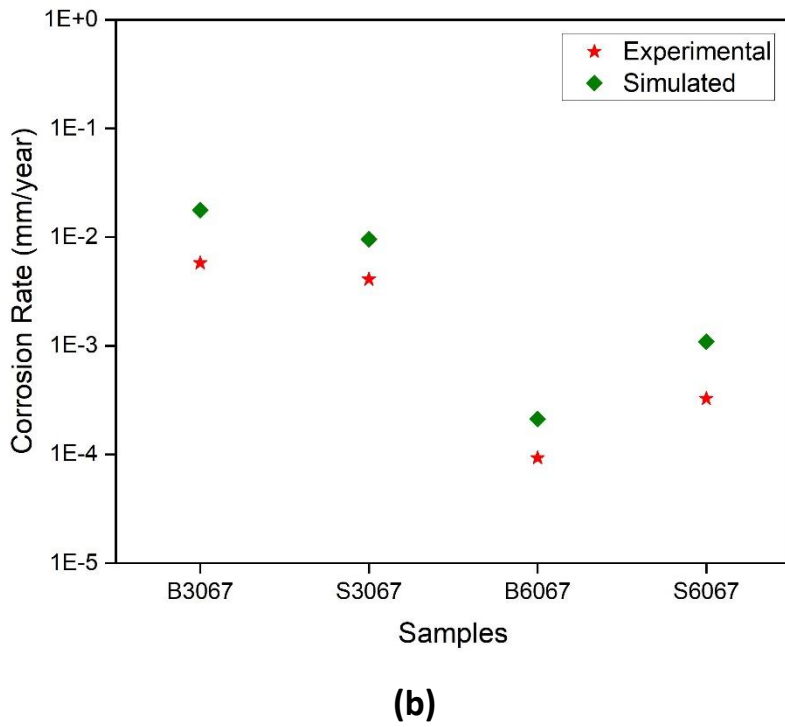
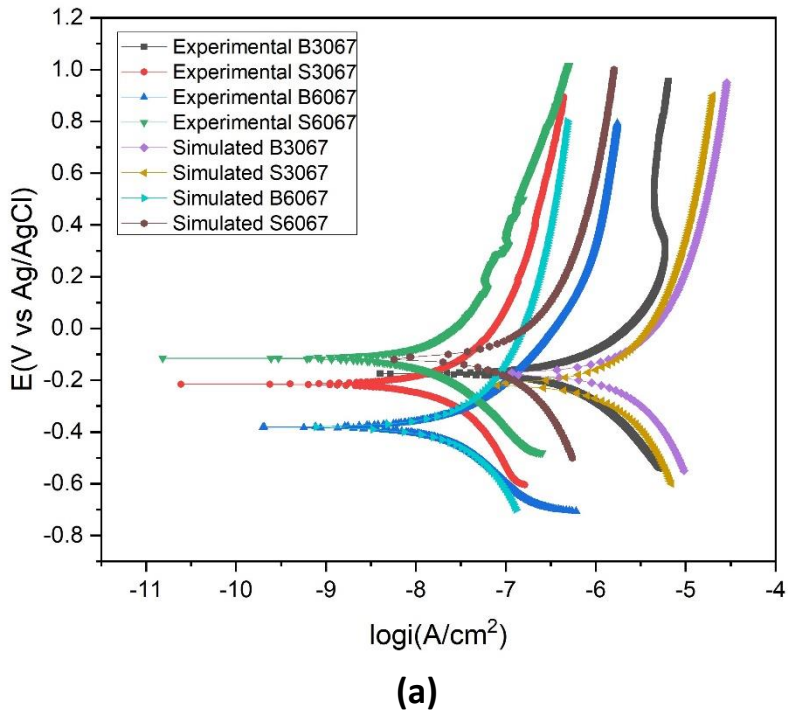


**Figure 6.6 Potentiodynamic polarization curve for SLM manufactured Ti-6Al-4V alloys (a) Corrosion rate comparison (b)**

## 7. Conclusions and Future Scope

The corrosion behaviors of Ti-6Al-4V samples manufactured by SLM in 3.5 wt.% NaCl solution was studied in this work. Further, the corrosion analysis is performed using COMSOL Multiphysics software to improve the understanding of the corrosion. These simulations are validated with the experiments before proceeding with the analysis. The main conclusions of the study are as follows:

- The microstructure of SLM-manufactured Ti-6Al-4V mainly consists of acicular and fine  $\alpha'/\alpha$  laths within the prior  $\beta$  grain boundaries. These laths are oriented at  $45^\circ$  to the prior  $\beta$  grain boundaries.
- The prior  $\beta$  grains morphology of the sample B3067 and B6067 is equiaxed whereas, for sample S3067 is columnar with the wall of jagged and discontinuous and for S6067 is short and irregular.
- A higher volume fraction of  $\alpha'$  is observed in 30  $\mu\text{m}$  thick powder bed samples due to the high cooling rates associated with them.
- The electrolyte potential for sample B3067 is more than that of other samples while B6067 has less electrolyte potential and other samples have electrolyte potential in between them. which means B3067 has higher tendency to get oxidized as compared to other samples.
- The electrolyte current density for sample B3067 is more than that of other samples while B6067 has less electrolyte current density and other samples have electrolyte current density in between them.
- The order of corrosion resistance of samples  $B3067 < S3067 < S6067 < B6067$  for both simulation and experimental approach.
- The corrosion rate calculated from the simulation for samples B3067, S3067, B6067, and S6067 is 3.05 times, 2.33 times, 2.26 times, and 3.37 times higher than that of experimentally calculated corrosion rate respectively.

## **Future Scope**

The research can be extended to achieve better corrosion resistance of Ti-6Al-4V alloys by some important studies:

- Effect of Vanadium (V) content on the corrosion resistance.
- Role of the  $\beta$  phase on the corrosion resistance.
- Effect of SLM parameters such as build orientation, laser scan rotation, etc.
- Role of microstructure on the corrosion behavior has to be ascertained.
- Influence of metastable  $\alpha'$  phase and prior  $\beta$  grains need to be investigated?
- Role of crystallographic texture generated during additive manufactured method also may influence the corrosion behavior which needs to be understood.

## 8. References

- [1] J. G. Zhou, "A new rapid tooling technique and its special binder study," *Rapid Prototyp. J.*, vol. 5, pp. 82–88, 1999.
- [2] R. Shrestha, J. Simsiriwong, and N. Shamsaei, "Fatigue Behavior of Additive Manufactured 316L Stainless Steel Parts: Effects of Layer Orientation and Surface Roughness," *Addit. Manuf.*, vol. 4, pp. 224–278, 2019, doi: 10.1016/j.addma.2019.04.011.
- [3] Chua C.K. and Leong K.F., "Rapid Prototyping Principles and Applications," in *World Scientific Publishing Co.Pte. Ltd.*, 2nd ed., singapore: World Scientific Publishing Co. Pte. Ltd., 2003.
- [4] D. Nimawat and M. Meghvanshi, "Using Rapid Prototyping Technology In Mechanical Scale Models," *Int. J. Eng. Res. Appl.*, vol. 2, pp. 215–219, 2012.
- [5] G. Sodeifian, S. Ghaseminejad, and A. Akbar, "Preparation of polypropylene / short glass fiber composite as Fused Deposition Modeling ( FDM ) filament," *Results Phys.*, vol. 12, pp. 205–222, 2019, doi: 10.1016/j.rinp.2018.11.065.
- [6] R. Anderl, H. Schmid, M. Kage, M. Cornelius, and H. Karg, *Additive Manufacturing*, no. June. 2017.
- [7] I. Gibson, "Additive Manufacturing Technologies," in *Rapid Prototyping to Direct Digital Manufacturing*, 2nd ed., singapore, 2010.
- [8] "INTRODUCTION TO Additive Manufacturing TECHNOLOGY," [Online]. Available: [www.epma.com/am](http://www.epma.com/am).
- [9] C. Palanisamy, "A review of additive manufacturing of  $\alpha$  -  $\beta$  Ti alloy components through selective laser melting and laser metal deposition," no. May, 2018.
- [10] E. Materials, *G. Lütjering, J.C. Williams, Titanium, Second ed.*, Springer, Berlin, 2007. .

- [11] S. Amirkhanlou, M. Ketabchi, and N. Parvin, "Proceedings of the 3rd Pan American Materials Congress," pp. 671–680, 2017, doi: 10.1007/978-3-319-52132-9.
- [12] J. Yang, H. Yang, H. Yu, Z. Wang, and X. Zeng, "Corrosion Behavior of Additive Manufactured Ti-6Al-4V Alloy in NaCl Solution," *Metall. Mater. Trans. A Phys. Metall. Mater. Sci.*, vol. 48, no. 7, pp. 3583–3593, 2017, doi: 10.1007/s11661-017-4087-9.
- [13] M. N. Gungor, K. R. Reasbeck, I. Uçok, L. S. Kramer, and H. Dong, "Microstructures and Mechanical Properties of Extruded and Cast Ti-6Al-4V," pp. 391–394, 2007.
- [14] R. Julien, V. Velay, V. Vidal, Y. Dahan, R. Forestier, and F. Rézai-Aria, "Characterization and modeling of forged Ti-6Al-4V Titanium alloy with microstructural considerations during quenching process," *Int. J. Mech. Sci.*, vol. 142–143, pp. 456–467, 2018, doi: 10.1016/j.ijmecsci.2018.05.023.
- [15] K. A. Natarajan, "Corrosion: Introduction – Definitions and Types," pp. 1–9, 2014.
- [16] A. Dalmau, V. Guiñón Pina, F. Devesa, V. Amigó, and A. Igual Muñoz, "Influence of fabrication process on electrochemical and surface properties of Ti-6Al-4V alloy for medical applications," *Electrochim. Acta*, vol. 95, pp. 102–111, 2013, doi: 10.1016/j.electacta.2013.01.155.
- [17] S. Bahl, S. Raj, S. Vanamali, S. Suwas, and K. Chatterjee, "Effect of boron addition and processing of Ti-6Al-4V on corrosion behaviour and biocompatibility," *Mater. Technol.*, vol. 29, no. B1, 2014, doi: 10.1179/1753555713Y.0000000118.
- [18] I. Cvijović-Alagić, Z. Cvijović, S. Mitrović, V. Panić, and M. Rakin, "Wear and corrosion behaviour of Ti-13Nb-13Zr and Ti-6Al-4V alloys in simulated physiological solution," *Corros. Sci.*, vol. 53, no. 2, pp. 796–808, 2011, doi: 10.1016/j.corsci.2010.11.014.

- [19] Z. Cai, T. Shafer, I. Watanabe, M. E. Nunn, and T. Okabe, “Electrochemical characterization of cast titanium alloys,” *Biomaterials*, vol. 24, no. 2, pp. 213–218, 2003, doi: 10.1016/S0142-9612(02)00293-4.
- [20] M. H. Abdulmageed and S. I. Ibrahim, “Corrosion Behavior of Ti-6Al-4V Alloy in Different Media,” *Al-Khwarizmi Eng. J.*, vol. 6, no. 3, pp. 77–84, 2010, [Online]. Available: <https://pdfs.semanticscholar.org/7c93/fb30658f10282435daa74a9beefe8b0fa9ad.pdf>.
- [21] C. M. Wu, “Accepted Manuscript,” 2015, doi: 10.1016/j.corsci.2015.10.041.
- [22] M. W. Steel *et al.*, “Effect of Si Content on the Corrosion Behavior of,” 2019.
- [23] B. Zhang, Y. Li, and Q. Bai, “Defect Formation Mechanisms in Selective Laser Melting: A Review,” *Chinese J. Mech. Eng. (English Ed.)*, vol. 30, no. 3, pp. 515–527, 2017, doi: 10.1007/s10033-017-0121-5.
- [24] N. T. Aboulkhair, N. M. Everitt, I. Ashcroft, and C. Tuck, “Reducing porosity in AlSi10Mg parts processed by selective laser melting,” *Addit. Manuf.*, vol. 1, pp. 77–86, 2014, doi: 10.1016/j.addma.2014.08.001.
- [25] P. Kumar, O. Prakash, and U. Ramamurty, “Acta Materialia Micro-and meso-structures and their influence on mechanical properties of selectively laser melted Ti-6Al-4V,” *Acta Mater.*, vol. 154, pp. 246–260, 2018, doi: 10.1016/j.actamat.2018.05.044.
- [26] A. A. B. Ruíz, *ASTM Standard G102-89, Calculation of Corrosion Rates and Related Information from Electrochemical Measurements*, vol. 3, no. 2. 2015.
- [27] COMSOL Multiphysics, *Electrochemistry module*, vol. 6, no. 9. 2003.

- [28] K. B. Deshpande, “Validated numerical modelling of galvanic corrosion for couples: Magnesium alloy (AE44)-mild steel and AE44-aluminium alloy (AA6063) in brine solution,” *Corros. Sci.*, vol. 52, no. 10, pp. 3514–3522, 2010, doi: 10.1016/j.corsci.2010.06.031.
- [29] N. Kazantseva, P. Krakhmalev, M. Thuvander, I. Yadroitsev, N. Vinogradova, and I. Ezhov, “Martensitic transformations in Ti-6Al-4V (ELI) alloy manufactured by 3D Printing,” *Mater. Charact.*, vol. 146, no. July, pp. 101–112, 2018, doi: 10.1016/j.matchar.2018.09.042.
- [30] T. Wang, Y. Y. Zhu, S. Q. Zhang, H. B. Tang, and H. M. Wang, “Grain morphology evolution behavior of titanium alloy components during laser melting deposition additive manufacturing,” *J. Alloys Compd.*, vol. 632, pp. 505–513, 2015, doi: 10.1016/j.jallcom.2015.01.256.
- [31] W. Xu, E. W. Lui, A. Pateras, M. Qian, and M. Brandt, “In situ tailoring microstructure in additively manufactured Ti-6Al-4V for superior mechanical performance,” *Acta Mater.*, vol. 125, pp. 390–400, 2017, doi: 10.1016/j.actamat.2016.12.027.